Economic Geology, v. 114, no. 6, pp. 1033–1056

The Metal Content of Magmatic-Hydrothermal Fluids and Its Relationship to Mineralization Potential

Andreas Audétat[1,†]

[1]*Bayerisches Geoinstitut, University of Bayreuth, 95440 Bayreuth, Germany*

Abstract

A fundamental question in the study of magmatic-hydrothermal ore deposits is whether the mineralization potential of intrusions was already predetermined by the metal content of the exsolving fluids. The present study aims at addressing this question by reviewing the large number of microanalytical data (mostly laser-ablation ICP-MS data) obtained on fluid inclusions from this type of ore deposits over the last 20 years. Published data sets were screened for analyses of high-temperature fluid inclusions that are representative of premineralization fluids. A set of criteria was developed to distinguish such fluids from later, lower temperature fluids. In order to compensate differences in absolute metal concentrations caused by fluid immiscibility, all element concentrations were normalized to Na. A numerical model was developed to explore at which stage different metals are most efficiently extracted from a cooling pluton. The results suggest that the timing of most efficient metal extraction varies from metal to metal and strongly depends on pressure, the fluid/melt partition coefficient and the bulk mineral-melt partition coefficient. As a consequence, fluid compositions were chosen over the entire range of Cs/Na ratios recorded from a given pluton, as this ratio gives an indication of the fractionation degree of the silicate melts from which a fluid exsolved. In order to avoid bias toward occurrences from which a large amount of data are available, maximum four intermediate-density (ID)-type fluid inclusion assemblages plus four brines assemblages were chosen from each occurrence.

Using the above-mentioned criteria, 169 fluid compositions from 12 Cu (Mo, Au) mineralized intrusions, 10 Sn/W mineralized intrusions, two Mo mineralized intrusions, and one U-Th-REE mineralized intrusion were finally chosen and plotted in graphs of X/Na versus Cs/Na. The results reveal that Sn- and Cu-mineralizing fluids contained more Sn and Cu, respectively, than the fluids analyzed from barren and Mo or U-Th REE mineralized intrusions. Positive correlations between fluid metal content and mineralization potential may exist also for W and REEs, whereas for Mo no such trend is evident. Therefore, at least for certain metals, the metal content of high-temperature fluid inclusions can be used as an indicator of the type and extent of mineralization. However, elevated metal concentrations are present also in some fluids from barren intrusions, which implies that the mineralization potential additionally depends on other factors such as the size of the intrusion and the development of structures that promote focused fluid flow.

Introduction

Magmatic-hydrothermal ore deposits are our main source of Cu, Mo, Sn, and W, and a major source of Au, Ag, Pb, and Zn (Kesler and Simon, 2015). By definition, magmatic-hydrothermal ore deposits are produced by hydrothermal fluids that are spatially and temporally associated with magma chambers. Although not all fluids in magmatic-hydrothermal systems are of magmatic origin but include also external fluids, such as meteoric water in the outer parts, the main source of the metals and transporting ligands (Cl, S, F) are the magmas themselves (e.g., Hedenquist and Lowenstern, 1994; Barnes, 1997). Knowledge of the metal and ligand content of magmatic-hydrothermal fluids is thus a key requirement to understand the formation of this economically important class of ore deposits, which comprises porphyry Cu (Mo, Au) deposits, porphyry Mo deposits, Sn-W granites, and intrusion-related polymetallic vein and skarn deposits.

The most direct record of metal transport and deposition by fluids in these deposits stems from fluid inclusions, which are small droplets of fluids that were trapped within minerals during or after crystal growth (e.g., Roedder, 1984; Shepherd et al., 1985; Goldstein and Reynolds, 1994; Goldstein, 2003; Samson et al., 2003). Information regarding the major components of fluids inclusions (bulk salinity, major salts, volatiles other than H_2O) have been obtained by means of microthermometry and Raman spectroscopy for more than 50 years (Roedder, 1984). Prior to 1998, only few data on the trace element content of fluid inclusions were available, which were obtained by either crush-leach analysis (e.g., Campbell 1995), proton-induced X-ray emission (e.g., Heinrich et al., 1992), or synchrotron X-ray fluorescence (e.g., Mavrogenes et al., 1995). A major breakthrough in laser-ablation inductively-coupled-plasma mass spectrometry (LA-ICP-MS) 20 years ago (Audétat et al., 1998; Günther et al., 1998) allows fast, routine analysis of major and trace elements in individual fluid inclusions down to the parts per million level. Thousands of fluid inclusions have been analyzed with this technique since then, most of them in samples related to magmatic-hydrothermal ore deposits. The aim of the present work is to provide a summary of LA-ICP-MS data obtained from high-temperature, premineralization fluid inclusions, in order to answer the fundamental question whether or not the mineralization potential of upper crustal intrusions was already reflected in the metal content of the related magmatic-hydrothermal fluids. An earlier treatment of this topic can be found in Audétat et al. (2008). The present study is based on a much larger database and includes constraints from a quantitative Rayleigh fractionation model.

[†]E-mail, Andreas.Audetat@Uni-Bayreuth.de

ISSN 0361-0128; doi:10.5382/econgeo.4673; 24 p.
Digital appendices are available in the online Supplements section.
Submitted: January 8, 2019 / Accepted: July 3, 2019

Methods

Choice of suitable samples

Since the focus of this study is on premineralization fluids and temperature is one of the most important factors controlling ore precipitation, it is critical to choose samples that formed at high temperatures. Most ores in porphyry Cu (±Mo, Au) systems, porphyry Mo systems, and Sn-W granites seem to have been precipitated at temperatures between 300° and 450°C (e.g., Heinrich, 1995; Redmond et al., 2004; Landtwing et al., 2005, 2010; Klemm et al., 2008; Kouzmanov and Pokrovski, 2012; Bodnar et al., 2014), but significant amounts of Bi, W, and Mo may have precipitated also at higher temperatures (e.g., Audétat et al., 2000a; Hart, 2007; Audétat and Li, 2017). It is thus necessary to choose fluid inclusion assemblages that were trapped at temperatures as high as possible. From now on, the term "high temperature" will be used for temperatures greater than ~450°C. One other important (but unfortunately often neglected) criterion is to choose samples that contain well-preserved fluid inclusions. Quartz is by far the most commonly studied host mineral due to its transparency, its relatively high strength, its resistance to alteration, and its wide distribution. However, despite its high strength and alteration resistance, quartz-hosted fluid inclusions commonly suffered from postentrapment modifications such as changes in fluid density and fluid salinity, which processes are commonly accompanied by fluid inclusion migration and/or dispersion within the host crystal (e.g., Mavrogenes and Bodnar, 1994; Audétat and Günther, 1999; Lambrecht and Diamond, 2014; Fall and Bodnar, 2018). The best samples to find well-preserved fluid inclusions that were trapped at high temperature are in euhedral quartz crystals from miarolitic cavities (Fig. 1a), as these cavities represent fluid pockets that developed during the last stages of magma crystallization (e.g., Olsen and Griffin, 1984; Audétat and Pettke, 2003). Suitable samples may also be found in high-temperature veins or breccias that contain quartz crystals that grew into open spaces, or in quartz grains that are surrounded by soft minerals such as sulfides, as the latter minerals can absorb mechanical stress. However, even fluid inclusions occurring in free-grown, euhedral quartz crystals commonly suffered from postentrapment modifications (Audétat and Günther, 1999), and it is critical to know which fluid inclusion properties can be trusted and which ones not. In general, the fluid density (determined primarily by the homogenization temperature) can very easily become modified through changes in the inclusion volume, whereas the fluid salinity (determined by the melting points of ice, clathrate or halite) seems to be a bit more difficult to change. Indications (although not unequivocal proof) of little or no postentrapment modifications are (1) occurrence of the fluid inclusions along well-defined trails or growth zones, (2) consistent microthermometric behavior within a given fluid inclusion assemblage, and (3) in the case of fluid entrapment in the two-phase field (see below), the occurrence of brine inclusions that reach total homogenization via bubble (rather than halite) disappearance (Audétat and Günther, 1999).

Fluid inclusion petrography

Most samples contain many different fluid inclusion assemblages that were trapped at various times during and after crystal growth (Fig. 1b). Depending on the mode of occurrence they may be classified into primary, pseudosecondary, and secondary (Roedder, 1984; Goldstein and Reynolds, 1994). A fluid inclusion assemblage is defined as a group of fluid inclusions that were trapped simultaneously, and thus, if trapped from a homogeneous fluid, have identical composition (Goldstein and Reynolds, 1994; Goldstein, 2003). Such fluid inclusions should show consistent phase proportions at room temperature (Fig. 1c) and show similar microthermometric behavior. If the fluid was two-phase (boiling) at the time of trapping, then two types of fluid inclusions (brine inclusions and vapor inclusions; ±mixed inclusions) may occur within a single assemblage (Fig. 1d). Such fluid inclusion assemblages are commonly called "boiling assemblages," and this term will be used hereafter. Once fluid inclusion assemblages have been identified, the next step is to reconstruct the entrapment sequence and to establish their time of formation relative to the mineralization by means of careful petrography. In xenomorphic quartz samples such as quartz veins, this task (including the classification of the fluid inclusion assemblages into primary, pseudosecondary, and secondary) should be accompanied by cathodoluminescence mapping, which technique allows visualization of growth zoning and multiple quartz generations in samples that otherwise look homogeneous (e.g., Rusk, 2012). To facilitate the reconstruction of the entrapment sequence it is helpful to review typical evolution paths followed by magmatic-hydrothermal fluids in upper crustal, intermediate to felsic intrusions (Fig. 2). Pivotal to Figure 2 are the facts that (1) the bulk fluids exsolving from such intrusions commonly have salinities of 5 to 15 wt % NaCl equiv (cf. Table 1 below), and (2) that during cooling from a magmatic temperature from 450° to 500°C the fluid pressure typically decreases from lithostatic pressure to about one-third to half of that value (Audétat and Pettke, 2003, Redmond et al., 2004; Audétat et al., 2008; Audétat and Li, 2017). Because the immiscibility region of the H_2O-NaCl model system overlaps partly with the solidus curve of granites, the physicochemical evolution of fluids within granitic intrusions depends critically on intrusion depth. Fluids that exsolve from deep intrusions (>6 km; corresponding to greater than ~1.5 kbars lithostatic pressure) are in the single-phase state at magmatic conditions (point A, Fig. 2a, b) and remain in this state during cooling to 500°C (point B, Fig. 2a, b). Consequently, all fluid inclusions trapped within this temperature interval show intermediate densities (i.e., a bubble volume fraction of 0.35–0.65 at room temperature; in the following called "ID-type fluid inclusions") and salinities of 5 to 15 wt % NaCl equiv.

Fluids that exsolve from plutons emplaced at intermediate depth levels (~4–6 km; corresponding to ~1.2–1.5 kbars) evolve from single phase at magmatic conditions (point A, Fig. 2c, d) to two phase at subsolidus conditions (point B, Fig. 2c, d). Due to the relatively low salinity of the parental single-phase fluid the two-phase field is generally intersected on the vapor limb (i.e., left of the critical curve in Fig. 2d), which means that small amounts of brine condense out of a vapor-like fluid. This fluid evolution path is followed in most mineralized systems (e.g., Hedenquist and Richards, 1998; Redmond et al., 2004; Williams-Jones and Heinrich, 2005; Audétat et al., 2008; Kouzmanov and Pokrovski, 2012), and also in many barren and subeconomically mineralized magma

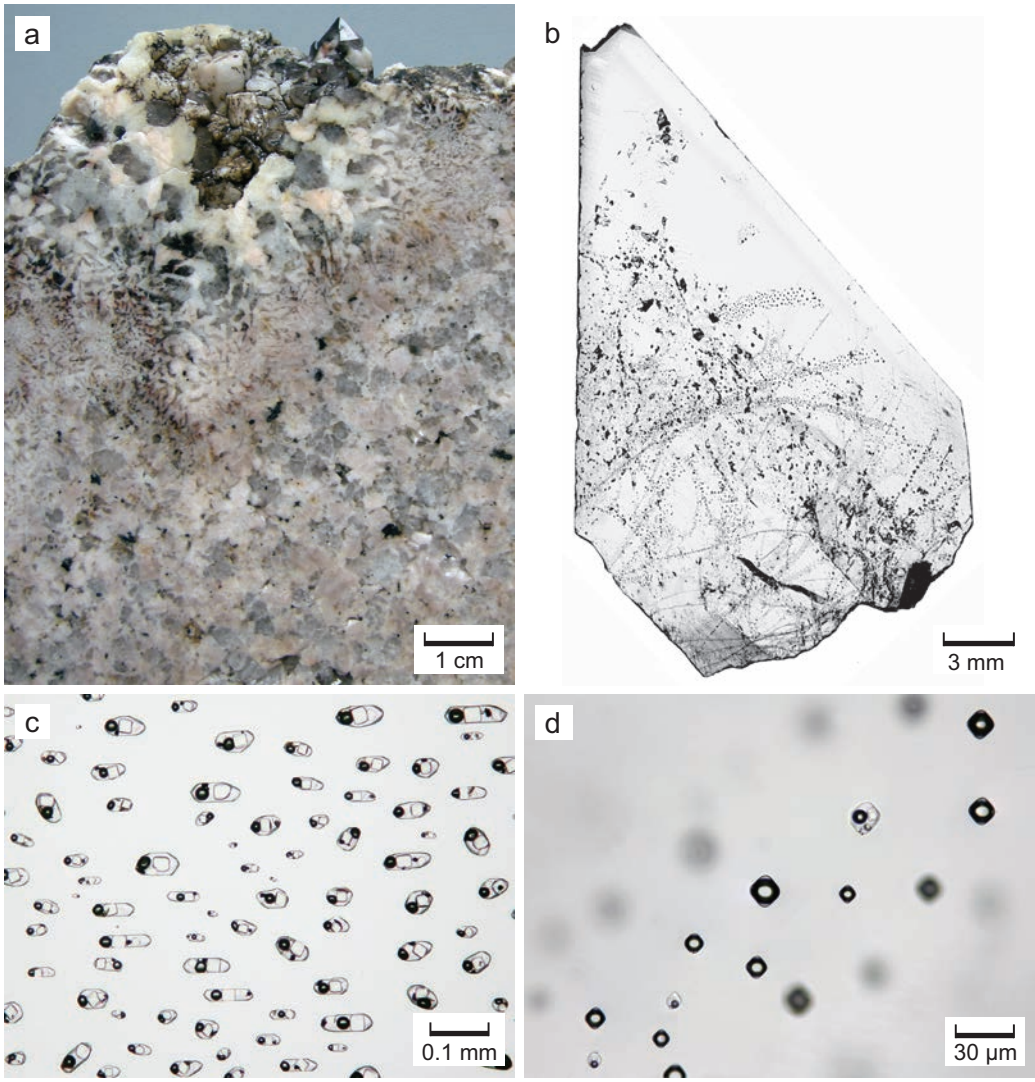

Fig. 1. (a). Section through a miarolitic cavity (sample Rito12 from the Rito del Medio Pluton, New Mexico, United States), showing the transition from coarse-grained granite (bottom) through fine-grained, granophyric texture and then pegmatitic texture to open-space mineralization within the cavity (top). (b). Transmitted-light image of a doubly polished thick section through one-half of a quartz crystal from a miarolitic cavity in the Erongo Granite, Namibia, showing several pseudosecondary fluid inclusion trails starting on former growth surfaces, plus large, irregularly distributed (but not primary) fluid inclusions in the core. (c). Photomicrograph of brine inclusions on a pseudosecondary trail in a quartz crystal from the MTE prospect on Capitan Mountains, New Mexico, United States. (d). Coexisting vapor-rich inclusions and brine inclusions on a pseudosecondary trail in a quartz crystal from the Trewhellas Lode, Mole Granite, Australia. The latter two photomicrographs were taken in transmitted light and were enhanced by focus stacking.

systems (e.g., Audétat and Pettke, 2003; Audétat et al., 2008; Lerchbaumer and Audétat, 2013). It needs to be noted that at temperatures below ca. 300° to 400°C many fluids become single phase again, either due to vapor contraction (Heinrich et al., 2004; Heinrich, 2005) or due to mixing with external meteoric water (e.g., Heinrich, 1990; Hedenquist and Richards, 1998; Ulrich et al., 2002). This low-temperature stage is not further discussed here because it starts after most of the Cu, Mo, Sn, and W precipitation.

Fluids exsolving from shallow plutons (<4 km; corresponding to less than ~1.2-kbar pressure) are already in the two-phase state at magmatic conditions, and they typically remain in the two-phase field during further cooling to 400° to 500°C (Fig. 2e, f). Vapor inclusions typically have very low densities, whereas brine inclusions typically have very high salinities, sometimes approaching the composition of nearly anhydrous salt melts.

Analytical techniques

Although this review is based on previously published data, it is important to provide a short description of the methods that are used to generate such data. The first step is to constrain the main components of a given fluid inclusion assemblage (fluid salinity, fluid density, major volatile phases) by means of microthermometry. In this technique, fragments of doubly polished thick sections are studied in a freezing-heating stage mounted on a microscope to record phase transition occurring within fluid inclusions during slow heating after prior cooling

Table 1. Overview of Sample Localities, Fluid Inclusion Characteristics, and Data Sources

Mineralization[1]	Occurrence	Sample type[2]	n[3]	ID-type FIs[4]	Salinity ID FIs wt % NaCl equiv	Coex. MIs[5]	Brines	T (°C)[6]	P (kbar)[6]	Data source
Barren	Rito del Medio (USA)	mc	6	+++	5-8	yes	+	700-720	1.1-1.3	Audétat et al. (2008); Zajacz et al. (2008); Audétat and Zhang (2019)
Barren	Cañada Pinabete (USA)	mc	5	+++	3-5	yes	+	600-720	1.0-1.3	Audétat and Pettke (2003); Audétat and Zhang (2019)
Barren	Huangshan (China)	mc	4	+++	4-7	yes	–	600-700	1.8	Audétat and Zhang (2018); Audétat and Zhang (2019)
Barren	Tongbei (China)	mc	3	+++	4-5	yes	+	(650-700)	(1.2-1.5)	Audétat and Zhang (2019)
Barren	Kirchberger (Germany)	mc	2	+++	7-8	yes	–	(610-660)	(1.9-2.2)	Audétat and Zhang (2019)
Barren	Eikeren (Norway)	mc	3	+++	6	yes	+	(620-680)	(1.5-1.8)	Audétat and Zhang (2019)
Barren	Baveno (Italy)	mc	n.a.	+++	6	yes	n.a.	650-670	1.9	Zajacz et al. (2008)
Barren	Mt. Malosa (Italy)	mc	5	–	n.a.	yes	+++	670-700	1.1-1.3	Zajacz et al. (2008)
Barren	Cuasso al Monte (Italy)	mc	n.a.	–	n.a.	yes	+++	690-720	0.8-1.0	Zajacz et al. (2008)
Barren (Mo)	Treasure Mt. Dome (USA)	mc	3	++	4-10	yes	+++	720	1.0	Lerchbaumer and Audétat (2013); Audétat and Zhang (2019)
Barren (Mo)	Drammen (USA)	mc	5	+++	6-10	yes	+	680-700	1.3-1.8	Lerchbaumer and Audétat (2013); Audétat and Zhang (2019)
Barren (Mo)	Glitrevann (Norway)	mc+v	3	+	5-12	no	+++	700	1.3	Lerchbaumer and Audétat (2013); Audétat and Zhang (2019)
Barren (Zn-Pb-Cu)	Stronghold (USA)	mc	4	++	3-6	yes	++	670-700	1.5-1.8	Audétat et al. (2008); Audétat and Zhang (2019)
Barren (Fe-Cu-Au-Ag)	Kofu Granite (Japan)	mc+v	5	+++	4-16	no	+	690-700	1.3-1.9	Kurosawa et al. (2010)
Cu-Au-Mo	Alumbrera (Argentina)	v	>30	+	5-10	no	+++	>600	0.7-1.2	Ulrich et al. (2002); Seo et al. (2009); Heinrich et al. (2011)
Cu-Au-Mo	Bingham (USA)	v	>30	++	6-10	no	+++	>550	0.9	Landtwing et al. (2005, 2010), Seo et al. (2012)
Cu-Mo-Au	Butte (USA)	v	>30	+++	2-5	no	+	550-700	2.0-2.5	Rusk et al. (2004, 2008)
Cu (Mo)	El Teniente (Chile)	v	>30	++	12-13	no	+++	n.a.	n.a.	Klemm et al. (2007)
Cu-Au (Mo)	Elatsitse (Bulgaria)	v	15	++	8	no	+++	≤730	1.2-1.3	Stefanova et al. (2014)
Cu-Mo-Au	Famantina (Argentina)	v	7	+	9-10	no	+++	n.a.	n.a.	Pudack et al. (2009)
Cu-Au (Mo)	Granisle (Canada)	v		n.a.	n.a.	no	+++	n.a.	n.a.	Wilson et al. (1980); Pettke (2008)
Cu-Au	Grasberg (Indonesia)	v		+	n.a.	no	+++	n.a.	n.a.	Ulrich et al. (1999); Williams-Jones and Heinrich (2005); Baline (2007)
Cu-Au (Mo)	Hillsboro (USA)	v	1	–	n.a.	no	+++	n.a.	n.a.	Audétat and Zhang (2019)
Cu-Mo	Organ Mts. (USA)	mc	3	–	n.a.	no	+++	n.a.	n.a.	Audétat and Zhang (2019)
Cu (Mo-Au)	Santa Rita (USA)	mc	1	–	≥20	yes	+++	700-740	1.2-1.4	Audétat et al. (2008); Audétat and Zhang (2019)
Cu-Mo	Yulong (China)	v	>30	++	6-12	no	+++	n.a.	n.a.	Chang et al. (2018)
Mo (Nb)	Cave Peak (USA)	mc+v	6	+	15-16	yes	+++	650-700	1.2-1.5	Audétat et al. (2008); Audétat (2010)
Mo	Questa (USA)	mhb+v	>30	++	2-8	no	++	n.a.	n.a.	Klemm et al. (2008)
Sn-W (Cu-Pb-Zn)	Mole Granite (Australia)	mc+v	>30	+	3-8	yes	+++	710-730	1.0	Audétat et al. (1998, 2000a,b, 2008)
Sn-W	Ehrenfriedersdorf (Germany)	peg	1	+++	7-9	yes	n.a.	680-710	1.0	Zajacz et al. (2008)

Table 1. *(Cont.)*

Mineralization[1]	Occurrence	Sample type[2]	n[3]	ID-type FIs[4]	Salinity ID FIs wt % NaCl equiv	Coex. MIs[5]	Brines	T (°C)[6]	P (kbar)[6]	Data source
Sn-W	Zinnwald (Germany)	mc+v	3	++	4-9	no	++	650-700	1.0-2.0	Graupner et al. (2005); Seo et al. (2009); Albrecht (2017)
Sn-W	Schellerhau (Germany)	pheno	n.a.	+++	9-11	no	+	n.a.	n.a.	Albrecht (2017)
Sn-W-U	Grummetstock (Germany)	v	1	++	9-13	no	++	n.a.	n.a.	Albrecht (2017)
Sn-Cu-As	Porth Ledden (England)	pheno	n.a.	++	n.a.	no	++	n.a.	n.a.	Albrecht (2017)
Sn-W	Industrial'noe (Russia)	mc	1	–	n.a.	no	+++	n.a.	n.a.	Naumov and Kamenetsky (2006)
W-Bi-Sn	Naegi Granite (Japan)	peg+mc+v	12	+++	5-8	yes	+	650-700	1.1-1.8	Yoshie (2012)
W-Bi-Mo	Ibara Granite (Japan)	peg+v	2	+++	4	yes	–	600-650	2.2-2.6	Yoshie (2012)
W	Erongo Granite (Namibia)	mc	1	–	n.a.	no	+++	n.a.	n.a.	Audétat and Zhang (2019)
Th-U-REE	Capitan Mts. (USA)	pheno+v	3	–	n.a.	yes	+++	≥700	<1 .0	Audétat et al. (2008); Audétat and Zhang (2019)

n.a. = not applicable or no information available
[1] Metals in parentheses are either subeconomic (in the case of "barren" systems) or byproduct (in the case of economic systems)
[2] mc = miarolitic cavity; v = vein; peg = pegmatite; pheno = magmatic quartz phenocryst
[3] Number of samples (not fluid inclusion assemblages) studied
[4] ID-type FIs = intermediate-density type fluid inclusions (+++ = abundant; ++ = medium; + = rare; – = none)
[5] Coex. MIs = coexisting melt inclusions present
[6] Estimated P-T conditions at the granite solidus; values in parentheses are less well constrained

to –50° to –100°C, until complete homogenization between all phases in a given fluid inclusion is attained. The results provide information on the bulk salinity (expressed as wt % NaCl equiv; i.e., the amount of dissolved NaCl if the fluid consisted of H_2O and NaCl only), the bulk density, the presence of significant amounts of gases such as CO_2, and in some cases on the relative proportion of major chloride components such as the NaCl/KCl ratio (e.g., Roedder, 1984; Shepherd et al., 1985). The identification and quantification of gases may be aided by Raman spectroscopy (Frezzotti et at., 2012). Subsequently, individual fluid inclusions are analyzed by LA-ICP-MS or Synchrotron-XRF. The vast majority of data used in this review were generated by LA-ICP-MS. Representative LA-ICP-MS signals obtained from ID-type fluid inclusions and brine inclusions are shown in Figure 3. In this technique, individual fluid inclusions are drilled out of their host (usually quartz) by means of a pulsed laser beam, and the resulting signals are integrated to obtain the bulk composition of each inclusion. The contribution of ablated quartz is numerically subtracted from the mixed signal until no Si is left. The latter step is essential for the quantification of Al, S, Cl, and Sn, which elements either occur in the quartz itself (Al, Sn) or are deliberated in the form of a contamination effect (S, Cl) from the interior walls of the sample chamber and the gas transport tube (Guillong et al., 2008; Seo et al., 2011; Fig. 3). Intensity ratios of the remaining signals are then converted into concentration ratios with the help of one or several external standards (usually a doped silicate glass such as NIST SRM 610; ±scapolite or afghanite for S and Cl). To convert the concentration ratios into absolute values an internal standard is required. This internal standard is commonly obtained by taking the microthermometrically determined NaCl equiv value and correcting it for other major cations (their abundance relative to Na being known from the LA-ICP-MS concentration ratios) to estimate the true Na concentration: $NaCl_{\text{"true"}}$ = NaCl equiv – 0.5 · ($KCl + FeCl_2 + MnCl_2 + CaCl_2$ + ...) (Heinrich et al., 2003). An alternative approach is to normalize the sum of all major cations expressed as chlorides (e.g., NaCl, KCl, $FeCl_2$) to the same molar Cl abundance as in the microthermometrically determined NaCl equiv value (Allan et al., 2005).

The two largest sources of uncertainty in this kind of analyses stem from imperfect sampling of the inclusion content, and from errors in the determination of the internal standard. The quality of the inclusion sampling depends on the one hand on the quality of the ablation process (the less controlled the ablation, the higher is the chance to lose parts of the inclusion content), and on the other hand on the representativeness of the signal sampling (due to the sequential analyses of isotopes/elements in quadrupole ICP-MS systems, very sharp signals may not be properly resolved). The uncertainty introduced by these two factors typically amounts to ~20% for elements that produce large signals (e.g., Günther et al., 1998; Heinrich et al., 2003) but is larger for elements close to the detection limit or ones that are strongly affected by the host correction. Inadequate instrumentation or improper ablation strategy may lead to higher uncertainties. For fluid inclusions that contain significant amounts of gases (e.g., CO_2) or that are dominated by salts other than NaCl, additional uncertainties arise due to the difficulty of constraining the internal

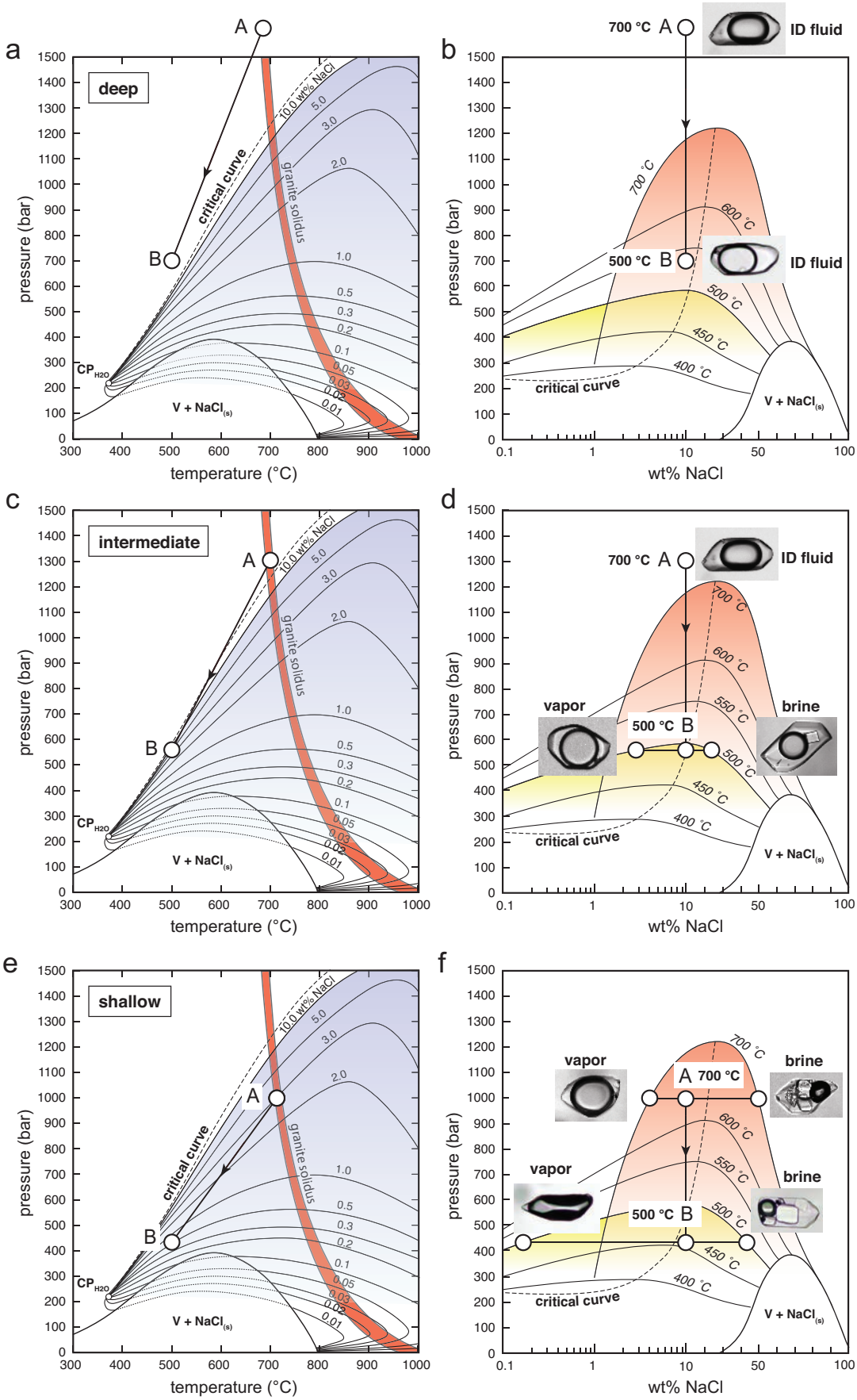

standard. These uncertainties can be very large (at least a factor of two) in certain cases, e.g., in ID-type or vapor-rich fluid inclusions that form clathrates upon freezing but do not contain liquid CO_2 at room temperature. The present study is focused mostly on concentration ratios, which are not affected by this latter source of uncertainty.

Selection of Specific Fluid Inclusion Assemblages

In order to avoid bias toward occurrences from which a large amount of data is available (e.g., Bingham Canyon; from which deposits more than 200 fluid inclusion assemblages have been analyzed), no more than eight fluid inclusion assemblages from each occurrence were selected for the forthcoming comparison. Consequently, criteria had to be developed to decide which fluid inclusion assemblages should be selected from larger databases. As will be explained in more detail below, these selection criteria include: (1) good fluid inclusion preservation; (2) selection of both ID-type and brine inclusions, where possible (maximum four each); (3) fluid entrapment at high temperature (>450°C; preferably >500°C); (4) data of fluid inclusion assemblages are preferred over data of single fluid inclusions; and (5) coverage of a large range of Cs concentration;

ID-type versus brine fluid inclusions

High-temperature ID-type fluids are the most obvious choice for the present comparison because these fluids represent premineralization, magmatic bulk fluids. However, for many occurrences no data on high-temperature ID-type fluids are available, either because such fluids were never present, or because corresponding fluid inclusions were destroyed or have not been recognized as such. Furthermore, many magmatic-hydrothermal systems show evidence for ore precipitation from two-phase fluids rather than from single-phase fluids, and the locus of mineralization often correlates with a high abundance of brine inclusions (e.g., Nash, 1976; Beane and Bodnar, 1995). It thus has been suggested that the formation of brines and their accumulation at depth might represent a critical step in the mineralization process (Audétat et al., 2008; Klemm et al., 2008). Due to these reasons it is desirable to also include brines in the comparison. However, this brings some difficulties.

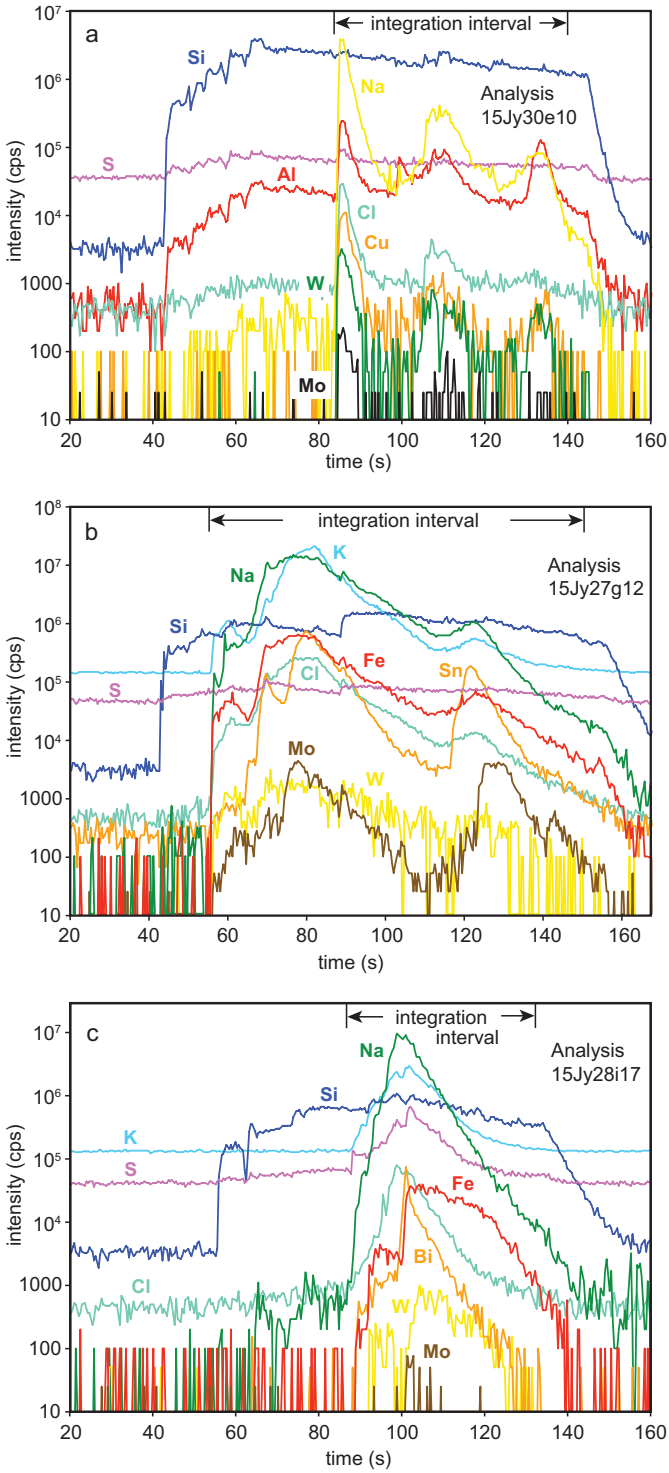

Fig. 2. Typical P-T-X evolution of magmatic-hydrothermal fluids in (a, b) deep, (c, d) intermediate, and (e, f) shallow intrusions. The panels on the left show outlines of the immiscibility fields of H_2O-NaCl fluids of various salinity projected onto the P-T plane (from Pitzer and Pabalan, 1986). The immiscibility field of a fluid with 10 wt % NaCl is highlighted in blue; above the blue area the fluid is single-phase; inside the blue area it is two-phase. Also shown is the solidus curve of fluid-saturated, granitic magmas (thick red line; compiled from Luth et al., 1964; Piwinskii and Wyllie, 1968; and Johannes and Holtz, 1996). The panels on the right show outlines of the immiscibility fields at various temperatures projected onto the P-X plane (from Bodnar et al., 1985; see also Driesner and Heinrich, 2007, for a more recent description of the H_2O-NaCl system). Immiscibility fields at 700°C and 500°C are highlighted in red and yellow, respectively. During cooling from 700°C to 500°C the fluid pressure typically drops by a factor of two to three. In deep intrusions, the fluids are single-phase field at both temperatures; in intermediate intrusions they are single-phase at magmatic conditions but two-phase at 500°C; whereas in shallow intrusions they are two-phase at both temperatures.

Fig. 3. LA-ICP-MS signals of fluid inclusions ablated through host quartz. (a). Signal of an ID-type inclusion of 50-μm size from the Huangshan granite, China (Huang18 trail C ID1; 6.0 wt % NaCl equiv; containing 2.1 wt % Na, 3.3 wt % Cl, 0.34 wt % Al, 290 ppm S, 190 ppm Cu, 31 ppm W, and 2 ppm Mo). (b). Signal of a brine inclusion of 55-μm size from the Erongo Granite, Namibia (Ero1E trailA brine 1; 50 wt % NaCl equiv; containing 36 wt % Cl, 12 wt % Fe, 10 wt % Na, 7.5 wt % K, 2,400 ppm Sn, 2,100 ppm W, and 38 ppm Mo). (c). Signal of a hypersaline brine inclusion of 25-μm size from the Treasure Mountain granite, Colorado, United States (60 wt % NaCl equiv; containing 28 wt % Cl, 17 wt % Na, 6.2 wt % K, 4.2 wt % S, 3.5 wt % Fe, 140 ppm Bi, 26 ppm W, and 1 ppm Mo).

Due to their higher salinity, brines are generally more metal rich than ID-type fluids, hence a comparison based on absolute metal concentrations would not be very helpful because it would just mimic the distribution of fluid salinities; i.e., occurrences that contain brines would appear more fertile than ones that contain only ID-type fluids (although, as mentioned above, the formation of brines may indeed be beneficial for mineralization). It is thus necessary to remove the effect of salinity by normalizing element concentrations to a constant fluid salinity or to a common major element such as Na. The two options lead to similar results because Na is usually the dominant cation in magmatic-hydrothermal fluids, hence, Na concentrations are proportional to fluid salinity (Fig. 4a). In the end, the element concentrations were normalized to Na because this does not rely on accurate measurement and interpretation of microthermometric data and can even be done if no constraints on fluid salinity are available. Remember that concentration ratios can be accurately (>5–7%) determined by LA-ICP-MS without the use of any internal standard. Two publications considered in this study do not report Na concentrations because Na cannot be quantified by SXRF in quartz-hosted fluid inclusions (Kurosawa et al., 2010, 2016). In these cases, a fictive Na concentration was calculated based on the average Na/(Na + K + Fe + Mn) concentration ratio of 0.6 determined in all other occurrences considered in the present study. There is no systematic difference in the salinity of ID-type fluids in barren versus variously mineralized intrusions (Fig. 4b), hence the normalization to Na should not introduce any artifact in the anticipated comparison of metal contents.

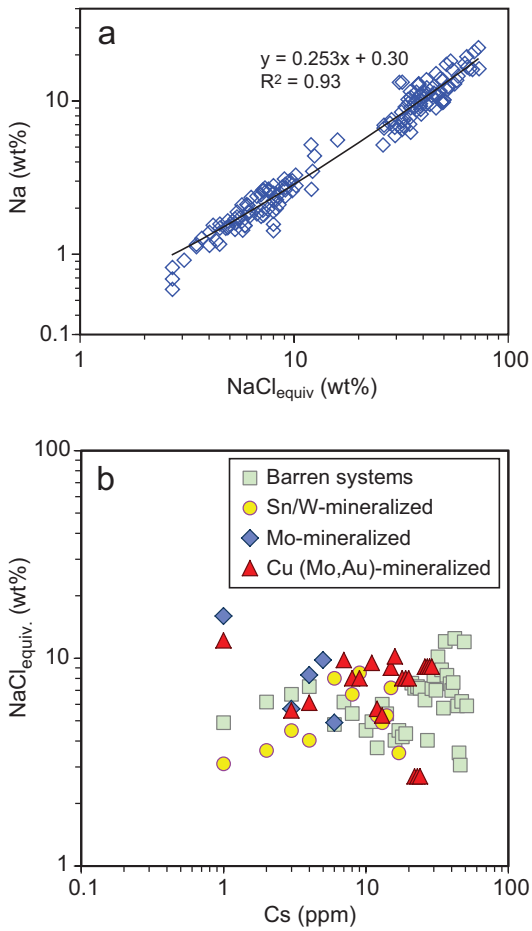

Fig. 4. (a). Correlation between microthermometrically determined fluid salinities and Na concentrations calculated based on the empirical correction formula of Heinrich et al. (2003) and Na/K/Fe/Mn ratios determined by LA-ICP-MS. (b). Salinity of ID-type fluids in barren versus variously mineralized intrusions. The Cs content of the fluid provides an indication of the degree of evolution of the silicate melt from which the fluid exsolved (see below).

Another difficulty of combining both ID-type fluid and brines is that the condensation of brine out of parental ID-type fluids is associated with element fractionation (Fig. 5). Fortunately, most elements show vapor/brine partition coefficients that are very similar to that of Na (dashed lines, Fig. 5), hence most element ratios do not change during vapor-brine separation. However, some elements such as Li, B, As, S, Cu, plus sometimes Sb, Mo deviate from this trend and are considerably shifted toward the vapor phase (Fig. 5; see also Heinrich et al., 1999; Williams-Jones and Heinrich, 2005; Seo et al., 2009; Pokrovski et al., 2013). In the case of Cu (and potentially also Li) the high vapor/brine partition coefficients determined on natural boiling assemblages hosted in quartz actually seem to be an artefact due to postentrapment diffusion of Cu into the vapor inclusions (Lerchbaumer and Audétat, 2012; Seo and Heinrich, 2013), but the other elements (B, As, S, ±Sb, ±Mo) are indeed depleted (on a Na normalized basis) in brines relative to ID-type precursor fluids.

Identification of high-temperature fluid inclusions

As mentioned above, one key criterion for the selection of fluid inclusion assemblages from larger data sets is that these assemblages were trapped at high temperature, i.e., at temperatures higher than 450°C.

In the case of deep-seated intrusions, in which all fluids trapped within the temperature interval of 400° to 70°C ultimately appear as ID-type fluid inclusions (Fig. 2b), high-temperature members are rather difficult to distinguish from lower temperature equivalents because they are petrographically and compositionally very similar. Neither their homogenization temperature nor their salinity tell much about their entrapment conditions. Indications for a high-temperature origin are (1) the presence of silicate daughter minerals (typically mica), (2) high Al contents (≥1,000 ppm) that are reproducible within a given fluid inclusion assemblage, (2) high contents of Bi, W and/or Mo compared to fluids with otherwise similar composition, at some localities, and (4) significant CO_2 contents, at some localities.

In shallower plutons, early, high-temperature ID-type fluid inclusions may look similar to later low-salinity fluids (i.e., contracted vapor or fluids with major meteoric component), but they usually have lower densities and may be distinguished from the latter ones using the same criteria as the ones listed in the previous paragraph. High-temperature brine inclusions may be distinguished from lower temperature ones by (1) high salinities (a salinity of 50 wt % NaCl equiv, for example, indicates an entrapment temperature of at least 450°C (Fig. 2)); (2) high homogenization temperatures (however, many high-temperature brine inclusions show artificially low homogenization temperatures due to postentrapment changes in fluid density; Audétat and Günther, 1999); and (3) elevated Al contents (>500 ppm).

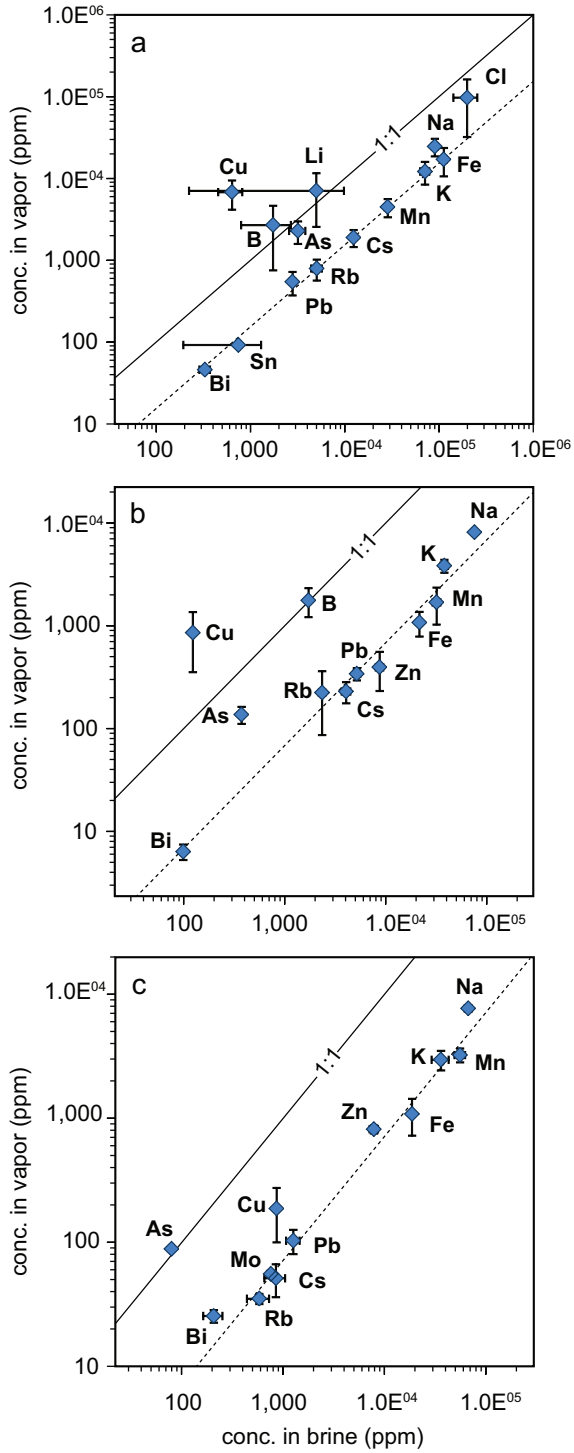

Fig. 5. Vapor-brine partitioning coefficients determined by LA-ICP-MS analysis of coexisting vapor and brine inclusions in natural boiling assemblages. (a). Assemblage Ero1A trailA from the Erongo Granite, Namibia (Lerchbaumer and Audétat, 2012; vapor: 6.7 wt % NaCl equiv; brine: 46 wt % NaCl equiv, $T_{h(total)(->l)}$ 470°C). (b). Assemblage Stro15B trailB from the Stronghold Granite, Arizona, United States (vapor: 2.7 wt % NaCl equiv; brine: 28.5 wt % NaCl equiv, $T_{h(total)(->l)}$ 510°C). (c). Assemblage Rito5 boil from the Rito del Medio Pluton, New Mexico, United States (Audétat and Pettke, 2003; vapor: 2.1 wt % NaCl equiv; brine: 29.5 wt % NaCl equiv, $T_{h(total)(->l)}$ 450°C). The stippled line shows the average partition coefficient of Cl-complexed elements; notice that Na always plots close to this line. The high apparent $D^{vapor/brine}$ values of Cu (and likely Li) are not real due to postentrapment diffusion of Cu into the vapor inclusions.

Based on these criteria the literature was screened for microanalytical data of high-temperature magmatic-hydrothermal fluids. An overview of the occurrences from which such data are reported is provided in Table 1. These occurrences include nine barren intrusions, five uneconomically Mo or base metal mineralized intrusions, and 25 intrusions that are mineralized with either Cu (±Mo, Au), Mo (±Nb), Sn (±W, base metals, U), W (±Bi, Sn, Mo) or Th-U-REE. Forty-nine out of the 169 ultimately chosen fluid compositions (mostly fluid inclusion assemblages, but 39 compositions represent single fluid inclusion analyses because no assemblages are reported) were taken from Audétat and Zhang (2019), who recently published a large new data set on the abundances of 38 major to trace elements in 124 high-temperature magmatic-hydrothermal fluids. Examples of well-preserved fluid inclusions analyzed in that latter study are shown in Figure 6.

Which high-temperature fluids best reflect the mineralization potential?

If one looks at the data available from a given occurrence, both ID-type fluid inclusions and brine inclusions typically show large compositional range, even if only high-temperature inclusions have been analyzed. It is thus critical to understand how these compositional variations relate to the mineralization potential, i.e., whether some fluids are more representative than others. To illustrate the problem, we take a look at two real examples: the barren Rito del Medio Pluton (New Mexico, United States), and the subeconomically Zn-Pb-Cu mineralized Stronghold Granite (Arizona, United States). For both occurrences, LA-ICP-MS data from eight to twelve ID-type fluid inclusion assemblages plus six to nine brine assemblages are available. The data are listed in Table 2. In order to save space, not all analyzed elements are listed, and only the average composition of each fluid inclusion assemblage is shown. In the Rito del Medio Pluton the concentrations of Mo and W in ID-type fluids range from 70 to 290 and from 6 to 33 ppm, respectively, whereas in brines they are 20 to 760 and 22 to 90 ppm, respectively. In the Stronghold Granite, the concentrations of Sn and Pb in ID-type fluids are 6 to 80 and 10 to 250 ppm, respectively, whereas in the brines they are 2 to 50 and 900 to 8000 ppm, respectively. Normalization to Na only slightly diminishes these large ranges in abundance. For the anticipated comparison it obviously matters whether one selects (1) only data from the lower end of these concentration ranges, (2) only data from the higher end, or (3) data that equally distributed over the whole range. Which fluids are most representative of the mineralizing fluid?

A very useful element to understand the origin of compositional variations in magmatic fluids is Cs because it reflects the fractionation degree of the silicate melt from which they exsolved (Audétat and Pettke, 2003; Audétat et al., 2008). The reason is that Cs is incompatible in most minerals and the partition coefficient of Cs between ID-type fluids and silicate melt is relatively close to unity (typically between 1 and 4; Fig. 7; see also Zajacz et al., 2008). In an earlier comparative study between barren and mineralized intrusions (Audétat et al., 2008) the focus was set on the least evolved fluids in each intrusion, based on the argument that the mass of fluids with low Cs contents is much larger than the mass of fluids with high Cs contents. However, as will be demonstrated, based

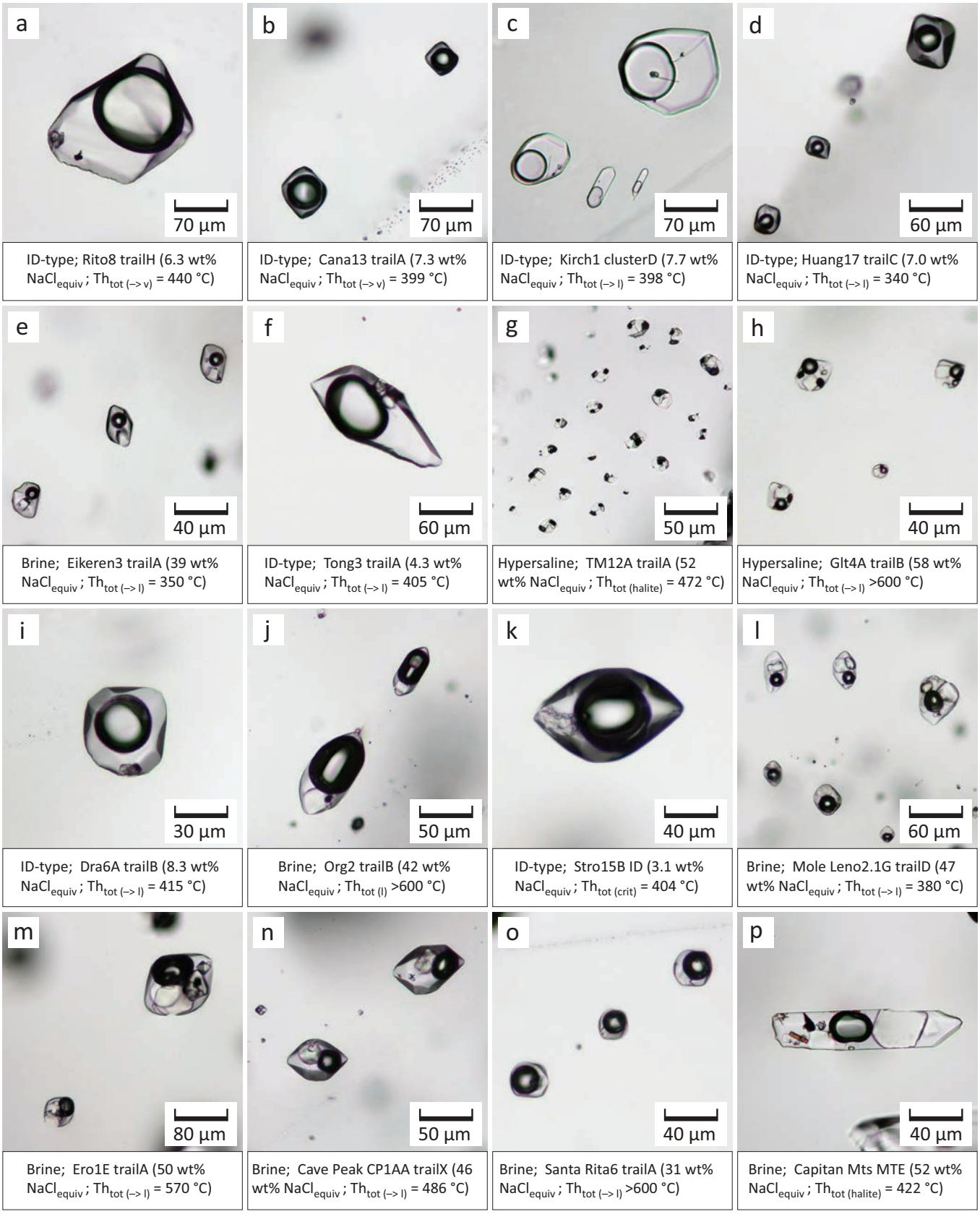

Fig. 6. Photomicrographs of fluid inclusions. All images were taken in transmitted light and were enhanced by focus stacking. $T_{h(total)\ (–> v)}$, $T_{h(total)\ (–> l)}$ $T_{h(total)\ (–> halite)}$ and $T_{h(total)\ (critical)}$ denote total homogenization into the vapor phase, into the liquid phase, via halite dissolution, or by critical behavior, respectively.

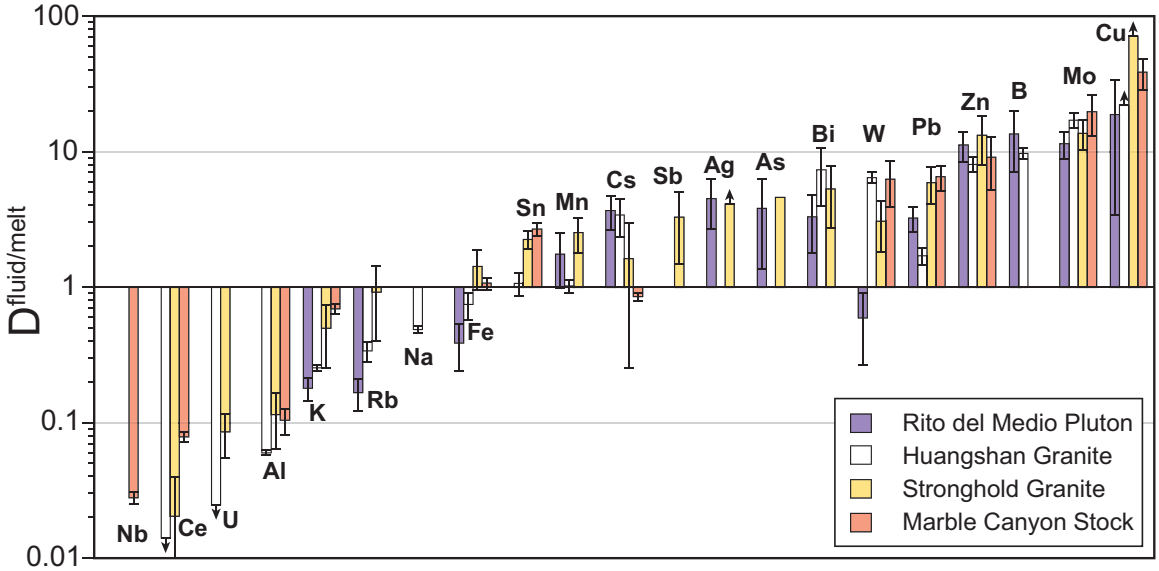

Fig. 7. Fluid/melt partition coefficients determined by LA-ICP-MS analyses of coexisting ID-type fluid inclusions and silicate melt inclusions in quartz crystals from miarolitic cavities. Rito del Medio Pluton: sample Rito5B LGZ; 700° to 720°C, 1.1 to 1.2 kbars, 4.9 wt % NaCl equiv in fluid (Audétat and Pettke, 2003). Huangshan granite: sample HS8A; 700°C, 1.8 kbars, 5.0 wt % NaCl equiv in fluid (Zhang and Audétat, 2018). Stronghold Granite: sample Stro1A; 675° to 700°C, 1.5 to 1.8 kbars, 5.9 wt % NaCl equiv in fluid (Audétat et al., 2008). Marble Canyon stock: sample MC2A-T; 650° to 700°C, 1.2 to 1.5 kbars, 17.5 wt % NaCl equiv in fluid (Audétat, 2010).

on a numerical model described below, this argument is not always valid because for certain metals and at certain pressure conditions the proportion of metal extracted at high degrees of crystallinity (i.e., by fluids with high Cs contents) is actually higher than the proportion of metal extracted at low degrees of crystallinity (i.e., by fluids with low Cs contents).

Figure 8 shows how the concentration of a hypothetical element X in the silicate melt evolves during open-system, fluid-saturated magma crystallization as a function of the fluid/melt partition coefficient and as a function of pressure. Element X is assumed to be 100% incompatible in the crystallizing minerals. At a pressure of 1 kbar, which corresponds to a water solubility of 4 wt % H_2O solubility in the silicate melt (Johannes and Holtz, 1996), fluid saturation leads to a decrease in the concentration of element X in the silicate melt (and, thus, also in the fluid) only if the fluid/melt partition coefficient is greater than 25 (Fig. 8a). At a pressure of 2 kbars, which corresponds to an H_2O solubility of 6 wt %, the threshold partition coefficient is 16.67 (Fig. 8b), and at 3.5 kbars (8 wt % H_2O solubility) it would be 12.5 (i.e., always 100 divided by the water solubility in wt %). If one compares these threshold values with the fluid/melt partition coefficients shown in Figure 7 results show that most elements will not become depleted in the residual melt during fluid-saturated crystallization of upper crustal plutons, unless they are to a significant degree incorporated in the crystallizing mineral assemblage. Exceptions are Mo and Cu, whose fluid/melt partition coefficients are commonly >15. However, the partition coefficient of Cu has to be treated with caution because the Cu content of natural, quartz-hosted ID-type fluid inclusions may be too high due to postentrapment diffusional gain of Cu (Lerchbaumer and Audétat, 2012).

With this principle at hand it is now possible to interpret the compositional variation of the data listed in Table 2. If one plots the composition of ID-type fluids as a function of their Cs content (i.e., against the degree of melt fractionation), then some prominent trends emerge (Fig. 9). In the Rito del Medio Pluton, the fluid salinity and the concentrations of most elements increase with increasing Cs content. In the Stronghold Granite, on the other hand, the fluid salinity and the concentrations of Cl-complexed elements such as Pb, Zn, and Sn decrease with increasing Cs content, whereas the concentrations of non-Cl-complexed elements such as Bi, Mo and W stay approximately constant (Mo, W) or increase (B, Bi). The contrasting behavior of the fluid salinity and the Cl-complexed elements in these two intrusions can be explained by the disparate pressures at which they crystallized (Rito del Medio Pluton: 1.2 ± 0.01 kbars; Stronghold Granite: 1.65 ± 0.15 kbars; Table 1). This occurs because $D_{Cl}^{fluid/melt}$ depends strongly on pressure. Based on experiments performed on haplogranitic melts at 810°C and 0.6 to 2.6 kbars, $D_{Cl}^{fluid/melt}$ is related to pressure by the following equation (Shinohara et al., 1989; Cline and Bodnar, 1991; pressure is given in kbar):

$$\log D_{Cl}^{fluid/melt} = -0.41288 + 1.8737 \cdot P - 0.48738 \cdot P^2 + 0.046511 \cdot P^3. \quad (1)$$

This equation returns a $D_{Cl}^{fluid/melt}$ value of 16 ± 3 for the pressure at which the Rito del Medio Pluton solidified (1.2 ± 0.1 kbars), which is smaller than the corresponding threshold fluid/melt partition coefficient value of 22 ± 1. For the Stronghold Granite, on the other hand, a $D_{Cl}^{fluid/melt}$ value of 36 ± 8 is obtained, which is larger than the threshold fluid/melt partition coefficient value of 19 ± 1 at a pressure of 1.65 ± 0.15 kbars. As a consequence, the fluid salinity and the concentration of Cl-complexed elements in the supercritical bulk fluid that exsolved from the Rito del Medio Pluton increased with increasing degree of fractionation, whereas in the Stronghold Granite they decreased. The threshold pressure at which

Table 2. Examples of How Fluid Compositions Were Selected from Larger Data Sets

FI assemblage[1]	Type[2]	n[3]	NaCl equiv (wt %)	$T_{h(total)}$ (°C)	Mode[4]	Na (ppm)	Al (ppm)	K (ppm)	Mn (ppm)	Fe (ppm)	Cu (ppm)	Zn (ppm)
ID-type fluids of the Rito del Medio Pluton												
Rito5 2GZ	ID	5	4.5	425	v/c	12,700	<400	9,400	2,400	600	260	n.a.
Rito5 LGZ*	ID	n.a.	4.9	420	c	12,100	1,000	6,900	3,500	4,100	70	900
Rito5 LGZ	ID	2	4.9	420	v/c	14,900	<100	6,700	2,500	2,100	80	700
Rito5 2GZ	ID	3	4.5	425	c	13,500	700	7,600	3,100	2,100	10	900
Rito8 trail A*	ID	2	6.7	420	v/c	18,300	2,500	8,700	7,000	4,300	1,800	1,600
Rito8 trail E	ID	2	4.9	430	v/c	13,700	300	4,300	5,500	1,600	<200	n.a.
Rito8 trail H	ID	2	6.3	440	v	19,500	1,200	6,100	3,900	2,300	1,300	1,000
Rito8 trail I*	ID	3	6.2	418	v	18,700	1,900	5,600	4,500	3,100	1,100	1,000
Rito3 trail A	ID	3	5.4	413	l	17,900	1,500	4,500	4,100	1,000	<10	800
Rito8 trail B	ID	2	6.4	440	c	18,900	1,500	9,100	4,800	2,200	2,000	1,800
Rito8 trail F	ID	3	7.5	n.a.	n.a.	20,200	3,700	8,600	8,300	5,100	2,600	1,700
Rito8 trail G*	ID	2	7.3	435	v/c	22,100	2,200	8,000	3,700	4,800	2,300	1,600
Brines of the Rito del Medio Pluton												
Rito8 trail C	B	n.a.	29.7	435	n.a.	95,000	n.a.	34,000	n.a.	18,600	1,300	n.a.
Rito8 trail C*	B	2	29.6	435	l	59,400	2,300	50,400	73,200	11,100	500	10,700
Rito3 trail B*	B	4	31.7	455	l	73,500	700	38,900	69,300	11,300	500	10,800
Rito5 trail B*	B	2	29.5	450	l	67,300	1,200	36,200	55,800	18,800	900	7,900
Rito8 trail D	B	n.a.	26.3	480	n.a.	81,000	n.a.	37,000	n.a.	18,300	1,200	n.a.
Rito8 trail D*	B	2	26.0	480	l	51,600	2,100	36,700	68,400	16,000	1,600	16,000
ID-type fluids of the Stronghold Granite												
Stro16B FI2,3*	ID	2	6.2	409	c/l	17,700	8,200	10,300	1,800	4,100	1,200	700
Stro1A 8-11*	ID	4	5.9	412	c/l	15,400	7,500	12,500	2,500	4,300	800	600
Stro16D ID	ID	3	5.4	407	c	16,500	1,200	7,400	1,300	3,200	1,900	600
Stro1B ID	ID	3	6.9	442	l	21,300	2,700	11,100	1,400	2,200	500	400
Stro16D FI1	ID	1	5.1	396	c	11,600	12,700	14,500	1,800	5,000	600	700
Stro15A FI1	ID	1	3.1	n.a.	n.a.	10,700	8,900	3,200	100	300	40	20
Stro15B ID*	ID	2	3.1	404	c	9,200	10,500	6,600	500	400	10	80
Stro15B FI1,2*	ID	2	3.5	n.a.	n.a.	11,200	14,400	6,600	300	400	90	100
Brines of the Stronghold Granite												
Stro15B tail F	B	2	31.2	445	l	78,000	700	46,800	24,500	35,300	40	4,400
Stro16A B1-3*	B	3	28.0	453	l	71,400	1,100	29,800	28,500	33,100	200	5,500
Stro15B trail C	B	4	27.6	454	l	63,200	100	51,900	29,500	27,200	200	5,600
Stro15B trail A	B	3	26.3	500	l	67,600	6,400	37,500	29,400	18,900	200	6,800
Stro15B trail E*	B	5	26.3	509	l	69,400	3,200	33,100	28,500	18,600	60	6,000
Stro15A FI2	B	1	26.2	n.a.	n.a.	68,100	8,100	40,700	23,000	21,200	100	5,400
Stro15B trail D	B	3	26.1	458	l	72,800	1,800	32,800	26,400	12,700	100	7,900
Stro15B trail B*	B	3	28.5	510	l	75,500	6,200	38,000	31,800	15,800	100	8,100
Stro1CC	B	1	31.6	460	l	106,000	n.a.	48,900	n.a.	43,400	10	n.a.

n.a. = not applicable or no information available

[1] FI = fluid inclusion; assemblages marked with a star are those that were chosen for the final database (i.e., for supplementary Table A1).

[2] ID = intermediate-density fluid; B = brine

[3] Number of fluid inclusions analyzed

[4] Mode of homogenization (v = homogenization into the vapor phase; l = homogenization into the liquid phase; c = critical homogenization by fading of the meniscus

[5] (1) = Audétat and Pettke (2003); (2) = Zajacz et al. (2008); (3) = Audétat and Zhang (2019); (4) = Seo et al. (2009); (5) Audétat et al. (2008)

the fluid salinity neither decreases nor increases is defined by the point at which $D_{Cl}^{fluid/melt}$ (eq (1) above) becomes equal to 100 divided by the water solubility in the melt in wt % (eq (2) below), which happens at 1.3 kbars.

Probably the best way to gain insights into the behavior of metals during magma crystallization and to understand at which stage a specific metal is extracted by the exsolving fluids is by means of numerical modeling. Therefore, a model similar to that of Cline and Bodnar (1991) was constructed, with the difference that the current model is not restricted to Cu but includes other economically important elements such as Mo, Sn, W, Bi, Pb, and Zn. The following variables were considered in this model: (1) the effect of pressure on the H_2O solubility in the silicate melt, (2) the effect of pressure on the fluid/melt partitioning coefficient of Cl (see above), and (3) the effect of fluid salinity on the fluid/melt partition coefficient of certain elements. Furthermore, the model allows use of fixed fluid/melt partition coefficients for those elements that are not complexed by chlorine, and to vary the bulk partition coefficient between the crystallizing minerals and the melt ($D_X^{bulk\ mineral/melt}$). The solubility of H_2O in haplogranitic melts at the eutectic point (Johannes and Holtz, 1996) at

Table 2. *(Cont.)*

FI assemblage1	Rb (ppm)	Mo (ppm)	Sn (ppm)	Cs (ppm)	W (ppm)	Pb (ppm)	Bi (ppm)	Mo/Na x1000	Sn/Na x1000	Cs/Na x1000	W/Na x1000	Pb/Na x1000	Data source5
ID-type fluids of the Rito del Medio Pluton													
Rito5 2GZ	110	70	<130	6	<31	n.a.	<31	6	<10.2	0	<2.4	n.a.	(1)
Rito5 LGZ*	143	130	30	50	11	200	12	11	2.5	4	0.9	17	(2)
Rito5 LGZ	88	130	<30	60	10	170	9	9	<2.0	4	0.7	11	(1)
Rito5 2GZ	161	170	<10	80	10	180	11	13	<0.7	6	0.7	13	(2)
Rito8 trail A*	160	220	<310	90	33	190	47	12	<16.9	5	1.8	10	(1)
Rito8 trail E	70	n.a.	<230	100	23	30	32	n.a.	<16.8	7	1.7	2	(1)
Rito8 trail H	113	120	<10	110	12	120	26	6	<0.5	6	0.6	6	(3)
Rito8 trail I*	122	180	<60	110	20	150	43	10	<3.2	6	1.1	8	(3)
Rito3 trail A	137	90	<10	120	6	170	26	5	<0.6	7	0.3	9	(3)
Rito8 trail B	180	180	<80	140	19	220	63	10	<4.2	7	1.0	12	(1)
Rito8 trail F	160	250	<190	140	30	210	48	12	<9.4	7	1.5	10	(1)
Rito8 trail G*	160	290	<110	160	26	240	63	13	<5.0	7	1.2	11	(1)
Brines of the Rito del Medio Pluton													
Rito8 trail C	n.a.	80	n.a.	720	n.a.	2,400	n.a.	0.8	n.a.	8	n.a.	25	(4)
Rito8 trail C*	900	20	<390	800	22	2,000	240	0.3	<6.6	13	0.4	34	(1)
Rito3 trail B*	1,000	250	<20	820	41	2,100	190	3.4	<0.3	11	0.6	29	(3)
Rito5 trail B*	580	760	<130	850	90	1,300	210	11.3	<1.9	13	1.3	19	(1)
Rito8 trail D	n.a.	130	n.a.	1,000	n.a.	2,300	n.a.	1.6	n.a.	12	n.a.	28	(4)
Rito8 trail D*	1,300	90	<340	1,300	54	2,200	250	1.7	<6.6	25	1.0	43	(1)
ID-type fluids of the Stronghold Granite													
Stro16B FI2,3*	550	30	60	100	70	180	17	1.7	3.4	6	4.0	10	(5)
Stro1A 8-11*	720	50	80	150	47	170	20	3.2	5.2	10	3.1	11	(1)
Stro16D ID	315	3	20	170	16	150	17	0.2	1.2	10	1.0	9	(3)
Stro1B ID	716	40	40	190	47	130	13	1.9	1.9	9	2.2	6	(3)
Stro16D FI1	1,700	<80	<150	300	28	250	16	<6.9	<12.9	26	2.4	22	(5)
Stro15A FI1	620	10	<10	930	12	10	15	0.9	<0.9	87	1.1	1	(5)
Stro15B ID*	932	30	6	2,400	37	50	58	3.3	0.7	260	4.0	5	(3)
Stro15B FI1,2*	1,600	40	<18	3,600	49	60	27	3.6	<1.6	320	4.4	5	(5)
Brines of the Stronghold Granite													
Stro15B tail F	1,710	1	4	980	10	900	31	0.0	0.1	13	0.1	12	(3)
Stro16A B1-3*	2,000	<80	<190	1,200	<44	1,400	33	<1.1	<2.7	17	<0.6	20	(5)
Stro15B trail C	1,942	<1	2	1,200	6	1,000	60	<0.0	0.0	19	0.1	16	(3)
Stro15B trail A	2,100	<10	<35	3,600	91	4,900	80	<0.1	<0.5	53	1.3	72	(5)
Stro15B trail E*	2,180	2	60	3,600	73	3,900	99	0.0	0.9	52	1.1	56	(3)
Stro15A FI2	2,132	<20	<38	3,600	140	2,700	78	<0.3	<0.6	53	2.1	40	(5)
Stro15B trail D	2,205	1	40	3,900	41	4,800	100	0.0	0.5	54	0.6	66	(3)
Stro15B trail B*	2,300	<10	50	4,000	69	5,200	99	<0.1	0.7	53	0.9	69	(5)
Stro1CC	n.a.	n.a.	n.a.	5,000	77	8,000	n.a.	n.a.	n.a.	47	0.7	75	(1)

pressures between 0.5 and 5.0 kbars can be approximated by the equation:

$$\text{Wt \% } H_2O = -0.1287 \cdot P^2 + 2.2762 \cdot P + 1.9888, \quad (2)$$

in which P is given in kbar. The effect of pressure on the $D_{Cl}^{fluid/melt}$ value is described by equation (1) above. Tests of equation (1) on experimental data published by Webster (1992) reveal that it works well in subaluminous melt systems containing 0.1 to 0.15 wt % Cl (i.e., the range of Cl concentrations observed in fluid-saturated, rhyolitic melt inclusions; Zajacz et al., 2008) at pressures to at least 2 kbars. This simple expression is thus adopted here even though it does not describe the change of $D_{Cl}^{fluid/melt}$ as a function of melt Cl content, nor takes into account the effect of fluid immiscibility. However, as demonstrated by Cline (1995), fluid immiscibility does not change much the general behavior of Cl-complexed elements and non-Cl-complexed elements during fluid-saturated magma crystallization.

The effect of fluid salinity on the fluid/melt partition coefficient of various metals has been investigated in numerous experimental studies, and it has been reviewed by Zajacz et

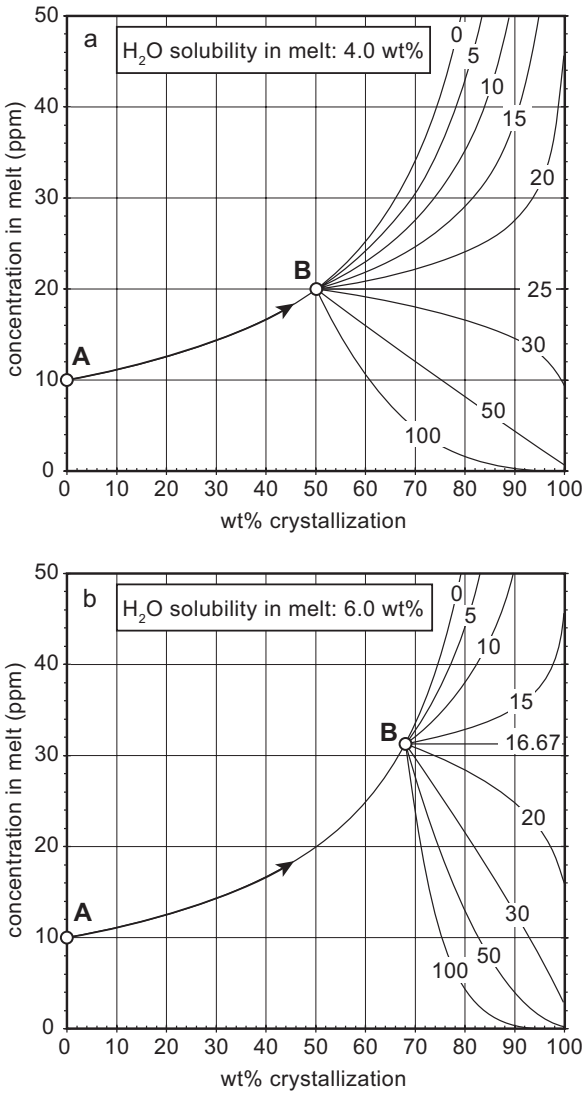

Fig. 8. Numerical model of the evolution of the concentration of element X in the silicate melt as a function of degree of magma crystallinity and the fluid/melt partition coefficient. For both graphs, the starting melt composition (point A) contains 2.0 wt % H_2O and 10 ppm of element X; element X is 100% incompatible in the crystallizing mineral phases, and each exsolving fluid batch is removed from the system (i.e., Rayleigh fractionation). (a). Model for magma crystallization at 1 kbar, at which pressure ca. 4 wt % H_2O can be dissolved in granitic silicate melts. Consequently, fluid saturation is reached at 50% crystallization (point B). Elements with fluid/melt partition coefficients $D_X^{fluid/melt}$ <25 become enriched in the residual silicate melt during further crystallization; elements with $D_X^{fluid/melt}$ >25 become depleted. (b). Same for magma crystallization at 2 kbars, at which pressure ca. 6 wt % H_2O can be dissolved in granitic silicate melts. In this case, fluid saturation is reached at 67wt % crystallization, and the threshold $D_X^{fluid/melt}$ deciding between enrichment or depletion in the residual silicate melt is 16.67 (=100 divided by the H_2O solubility in the silicate melt).

al. (2008) in their study on natural assemblages of coexisting melt and fluid inclusions in quartz crystals from miarolitic cavities. Zajacz et al. (2008) grouped the metals into (1) those that display a strong positive correlation between $D_X^{fluid/melt}$ and fluid salinity, (2) those that display only a moderately positive correlation, and (3) those that display none or even a negative correlation with fluid salinity. In keeping with their observations, $D_{Pb}^{fluid/melt}$ was thus modeled to be related by a factor of six to the Cl molality of the fluid ($D_{Pb}^{fluid/melt} = 6 \cdot m_{Cl}^{fluid}$), $D_{Zn}^{fluid/melt}$ was modeled to be related by a factor of eight ($D_{Zn}^{fluid/melt} = 8 \cdot m_{Cl}^{fluid}$), $D_{Sn}^{fluid/melt}$ by a factor of two ($D_{Sn}^{fluid/melt} = 2 \cdot m_{Cl}^{fluid}$), whereas $D_B^{fluid/melt}$, $D_{Mo}^{fluid/melt}$, $D_W^{fluid/melt}$, and $D_{Bi}^{fluid/melt}$ were assumed to be independent of fluid salinity. However, in contrast to the study of Zajacz et al. (2008), $D_W^{fluid/melt}$ was assumed to be independent of fluid salinity (their data do not allow firm conclusions). The fluid/melt partition coefficient of Cs was set to a constant value of 3 (Fig. 7). Boron, Mo, W, and Bi were assumed to be 100% incompatible in the crystallizing minerals (i.e., $D_X^{bulk\ minerals/melt} = 0$), whereas $D_{Zn}^{bulk\ minerals/melt}$ was assumed to be 0.2, $D_{Pb}^{bulk\ minerals/melt} = 0.4$, and $D_{Sn}^{bulk\ minerals/melt} = 0.5$. The starting concentrations of the metals in the silicate melt were chosen based on values measured in silicate melt inclusions (Audétat and Pettke, 2003; Audétat et al., 2008; plus a few unpublished data from the Stronghold Granite), but in principle they do not matter because the slopes of the trends do not depend on absolute metal concentrations. All calculations were performed for the case of open-system fractional crystallization (i.e., Rayleigh fractionation), in steps of 1 wt % crystallization.

The model was first tested on the Rito del Medio Pluton and the Stronghold Granite, for which constraints on the P-T conditions and the behavior of metals during fractional crystallization are available. The results of the calculations are presented in Figure 10. The model reproduces nearly all trends shown in Figure 9, i.e., in the Rito del Medio Pluton both the fluid salinity and all metal concentrations increase with increasing Cs content of the fluid, whereas in the Stronghold Granite the fluid salinity and the concentrations of Cl-complexed elements (Pb, Zn) decrease and the concentrations of the non-Cl-complexed elements Mo and Bi remain ±constant. The only element that shows a discrepancy in its qualitative behavior is W, the concentration of which is predicted to increase with increasing fractionation in both plutons, whereas in the Stronghold Granite the actually measured concentrations remain ±constant. Apparently, W behaved incompatibly with respect to the crystallizing minerals in the Rito del Medio Pluton, but compatible in the Stronghold Granite. The reason for the stronger decrease in the modeled fluid salinity in the Stronghold Granite is not known. However, considering the simplicity of the model the otherwise good match between modeled and actual behavior is satisfactory.

Importantly, the model allows determination of the total amount of metal extracted at each crystallization interval, which information cannot be obtained from the fluid composition itself. The principle is illustrated on Mo in the Rito del Medio Pluton (Fig. 11). In a first step, the concentrations of Mo and Cs in the exsolving fluid at each crystallization interval was calculated (Fig. 11a). In a second step, the cumulative percentage of extracted metal was calculated for each crystallization degree (Fig. 11b). Finally, the results of the first two steps were combined in a plot of Mo concentration in the fluid versus Cs concentration in the fluid (Fig. 11c), which is similar to the type of plots shown in Figures 9 and 10. In this way it is possible to see at which Cs concentration in the fluid most of the Mo is extracted. The result suggests that 50% of the entire Mo budget is extracted by fluids that contain ≥22 ppm Cs and

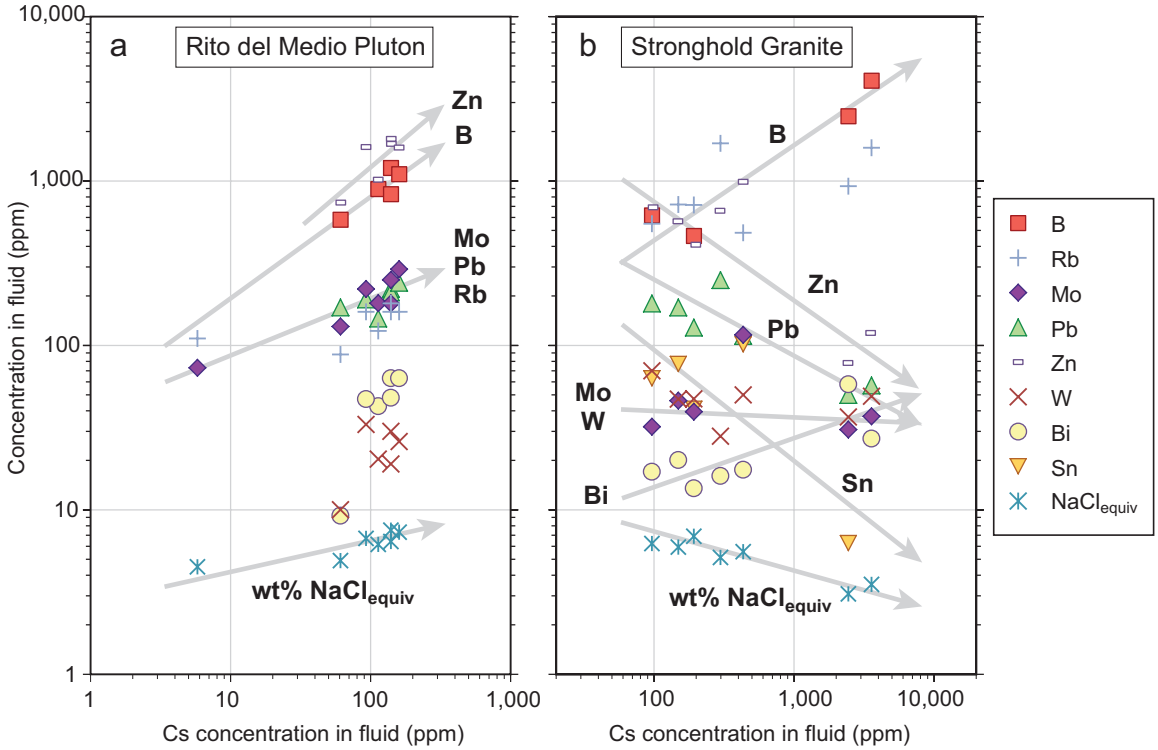

Fig. 9. Composition of ID-type fluids as a function of their Cs content. (a). In the Rito del Medio Pluton, which crystallized at 1.1 to 1.2 kbars, the fluid salinity and the concentration of Cl-complexed elements such as Pb and Rb increased with increasing degree of melt fractionation. (b). In the Stronghold Granite, which crystallized at 1.5 to 1.8 kbars, the fluid salinity and the concentration of Cl-complexed elements such as Pb and Sn decreased with decreasing fluid salinity, whereas the concentrations of non-Cl-complexed elements such as W, Bi, Mo, and B remain stable or increase.

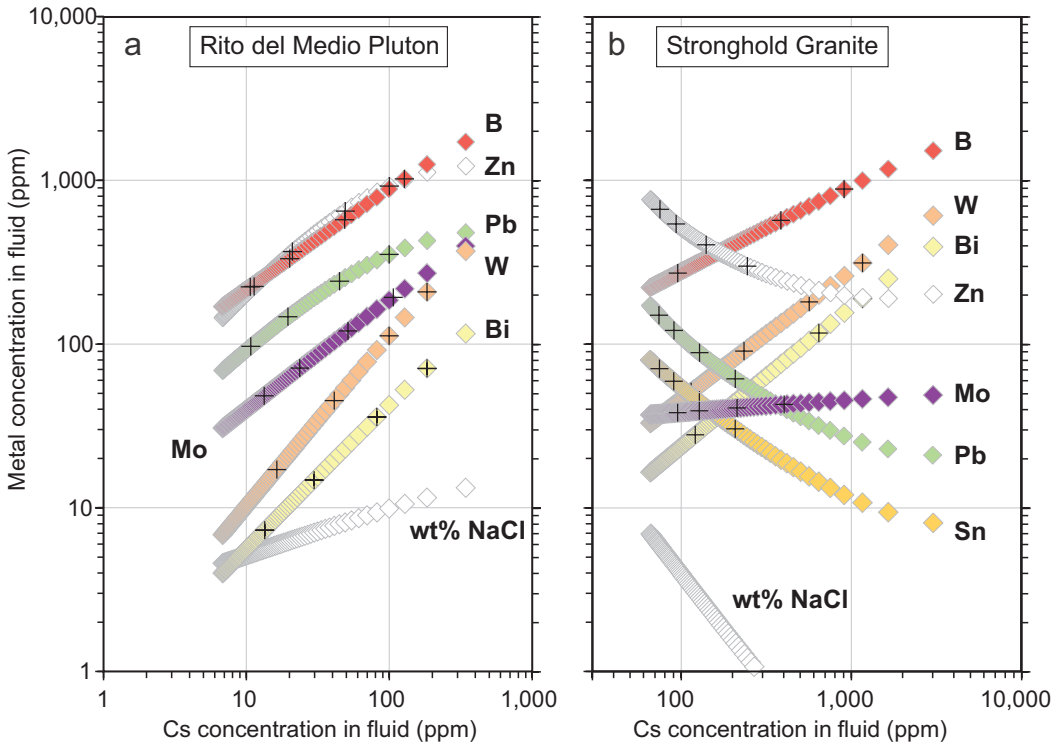

Fig. 10. Modeled evolution of single-phase, magmatic fluids exsolving from the Rito del Medio Pluton and the Stronghold Granite, using the constraints and equations discussed in the text. The crosses denote (from left to right) 25, 50, 75, and 90% cumulative extraction percentages for each element.

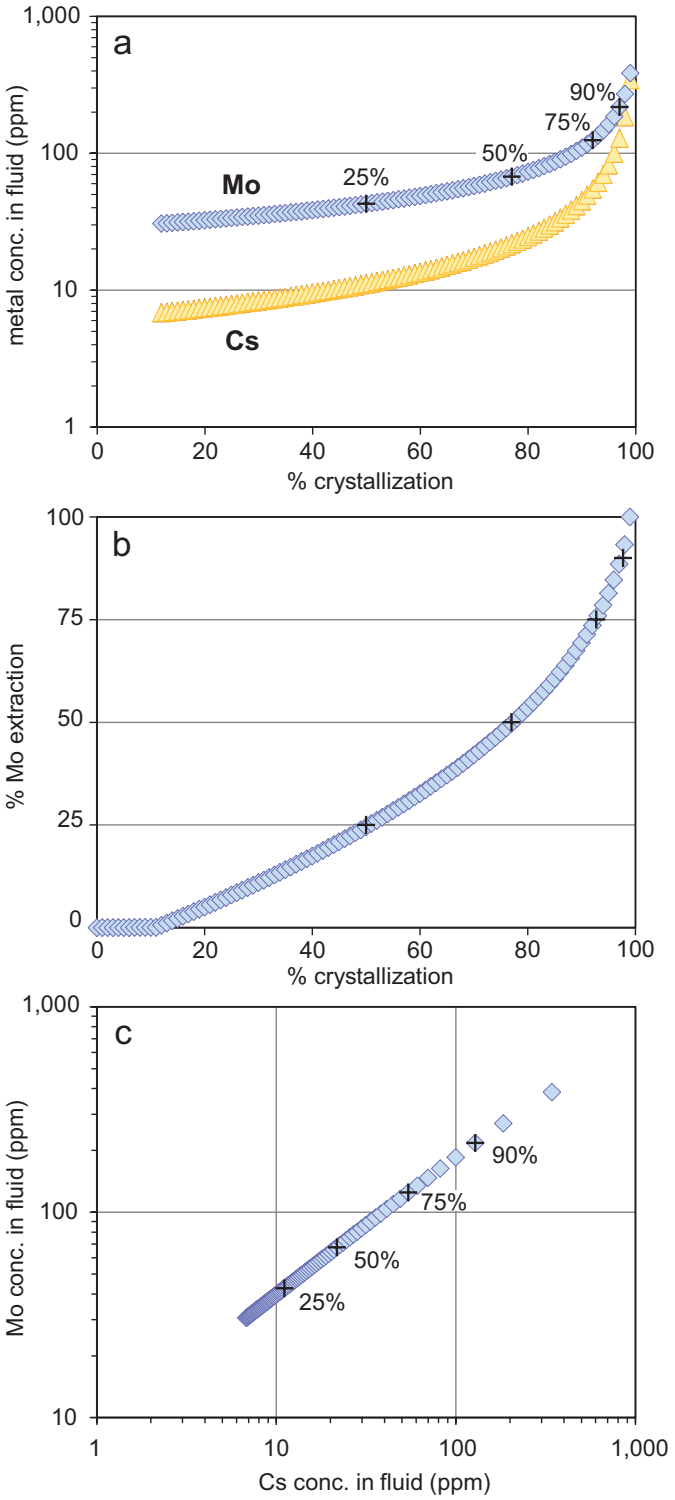

Fig. 11. Modeled Mo and Cs concentrations in the fluids exsolving from the Rito del Medio Pluton. (a). Absolute Mo and Cs concentrations as a function of the degree of magma crystallization. (b). Cumulative percentages of the total amount of extracted Mo as a function of the degree of magma crystallization. The crosses mark the stages at which 25, 50, 75, and 90% cumulative extraction are reached. These stages are marked also in the other panels. (c). Mo concentration as a function Cs concentration. The graphs suggest that 50% of all Mo is extracted at >77% magma crystallization, by fluids containing >22 ppm Cs. Fluids containing ≥60 ppm Cs (i.e., most of the data points in Fig. 9a) transport 25% of the total extracted Mo.

exsolved at ≥77% crystallization (the latter information be extracted from Fig. 11a). Even fluids that contain ≥100 ppm Cs and exsolved at ≥96% crystallization still account for 15% of the total Mo budget, i.e., in this example, highly evolved fluids should not be neglected despite their relatively low total mass compared to less evolved fluids.

Cumulative extraction percentages of 25, 50, 75, and 90% total metal are also shown for all elements displayed in Figure 10. The results suggest that in the Rito del Medio Pluton ≥50% of the total B, Zn, Pb, Mo, W, and Bi were extracted by fluids containing ≤40 ppm Cs, but that fluids containing ≥60 ppm Cs still transported 24 to 42% of the total metal. A similar conclusion can be made for the Stronghold Granite, where ≥50% of the total Zn, Pb, Sn, and Mo were extracted by fluids containing ≤120 ppm Cs, whereas 25 to 40% of the total amount of extracted B, W, and Bi were transported by fluids containing ≥390 ppm Cs.

A more systematic treatment on the effects of pressure, fluid/melt partition coefficient, and bulk mineral-melt partition coefficient is provided in Appendix Figure A1. For this purpose, four contrasting metals were considered: (1) Pb as an element that shows a strong affinity to Cl and displays a high fluid/melt partition coefficient; (2) Rb that shows a significant affinity to Cl but displays a low fluid/melt partition coefficient; (3) Mo that shows no affinity to Cl and displays a high fluid/melt partition coefficient; and (4) W that shows no affinity to Cl and displays a lower fluid/melt partition coefficient. The behavior of each of these elements was modeled at pressures of 0.5, 1.0, and 2.0 kbars. The results (App. Fig. A1) suggest that Cl-complexed elements such as Pb and Rb are dominantly extracted by late (i.e., Cs-rich) fluids at 0.5 and 1.0 kbar, but dominantly extracted by early (i.e., Cs-poor) fluids at 2.0 kbars. In all cases, the efficiency of Pb and Rb extraction correlates with the Pb and Rb content of the fluid, i.e., most Pb and Rb is extracted by Pb- and Rb-rich fluids. Molybdenum tends to be extracted by early fluids, which in the case of 2 kbars corresponds also to the most Mo rich fluids. However, at 0.5 and 1.0 kbar a larger proportion of Mo is actually extracted by relatively Mo poor fluids. Tungsten is extracted continuously over the entire crystallization interval at all three pressures but nevertheless becomes enriched in the residual melt, suggesting that early, Cs- and W-poor fluids are similarly important as late, Cs- and W-rich fluids. The effect of increasing the bulk mineral-melt partition coefficient is that a higher percentage of metal is extracted by early fluids, i.e., a metal that may be extracted dominantly by late fluids at low $D_X^{\text{bulk minerals/melt}}$ may be extracted dominantly by early fluids at high $D_X^{\text{bulk minerals/melt}}$.

In summary, the results suggest that the extraction of metals from crystallizing magmas is relatively complex and that no single type of ID fluid (neither the least evolved one, nor the most evolved one, nor the most metal rich one) can be regarded as representative for all elements. Consequently, in the present study fluid compositions spread over the entire interval of recorded Cs/Na ratios were chosen for the comparison. More precisely, up to four ID-type fluid compositions plus up to four brine compositions were selected, both spread over a large Cs/Na interval. Further selection criteria include: (1) evidence for a high-temperature origin (i.e., high Al content; high salinity, high homogenization temperature),

(2) trustworthiness of the data (number of fluid inclusions analyzed, reproducibility of results), and (3) range of elements analyzed (with priority given to Cu, Mo, Sn, W, Ce, and Cs, which are the elements of main focus in the present study). Applying these criteria to Table 2, four ID-type fluid compositions and four brine compositions from the Rito del Medio Pluton were selected, and four ID-type fluid compositions and three brine compositions from the Stronghold Granite (Table 2). The reason why the least evolved ID-type fluid of the Rito del Medio Pluton was not selected is that its Al content is low and that the Sn and W concentrations are below the detection limit. The reason why only three instead of four brine compositions were chosen from the Stronghold Granite is that most of the analyzed brine compositions are extremely evolved, hence they can represent only a small part of the fluid spectrum.

Miarolitic cavities versus hydrothermal veins

Because many of the fluid inclusion analyses used in this comparison were obtained in samples from miarolitic cavities, which are known to form relatively late in the crystallization history of magmas, we need to test whether the fluids trapped in such samples are actually representative of those exsolving from the bulk intrusion. If fluid saturation was reached relatively early in the crystallization history of the intrusion, it is conceivable that the quartz crystals from miarolitic cavities record only highly evolved fluids that are not representative of the average fluids exsolved from it. On the other hand, if the intrusion incrementally crystallized from rim to core and miarolitic cavities did not behave as closed systems, then miarolitic cavities located near the roof of the intrusion (which is where they typically developed) may also have "seen" fluids that exsolved from less fractionated melt portions below.

This question can be tested on several intrusions from which data from both miarolitic cavities and from mineralized veins are available: (1) the Sn-W mineralized Mole Granite, (2) the W-Bi-Sn mineralized Naegi granite, and (3) the weakly Mo mineralized Glitrevann granite (Table 1). In the Mole Granite, early ID-type fluids and subsequent two-phase fluids (i.e., vapor + brine) were trapped in a miarolitic cavity, whereas only two-phase fluids were trapped in mineralized veins. Figure 12a thus compares Na normalized element abundances in 13 high-temperature brine assemblages analyzed from the miarolitic cavity with those of 18 high-temperature, premineralization brine assemblages analyzed from eight different mineralized veins. Within the quoted uncertainties (which correspond to 1σ standard deviations of the mean of all assemblages), all elements occur at similar concentrations in both types of samples, suggesting that brines trapped in miarolitic cavities are representative of potentially ore-forming fluids. In the Naegi granite, mostly ID-type fluids were found in pegmatite pockets, and both ID- fluids and subcritical brine + vapor fluids were analyzed in mineralized veins. The compositions of three ID-type fluids from a pegmatite pocket are thus compared with 12 ID-type fluids from five different veins (Fig. 12b). Again, all element abundances agree within the quoted uncertainties, although the latter are rather large (the apparent discrepancy in Cu concentrations may be due to various extents of postentrapment Cu gain). In the Glitrevann granite, 10 ID-type fluids analyzed from two different miarolitic

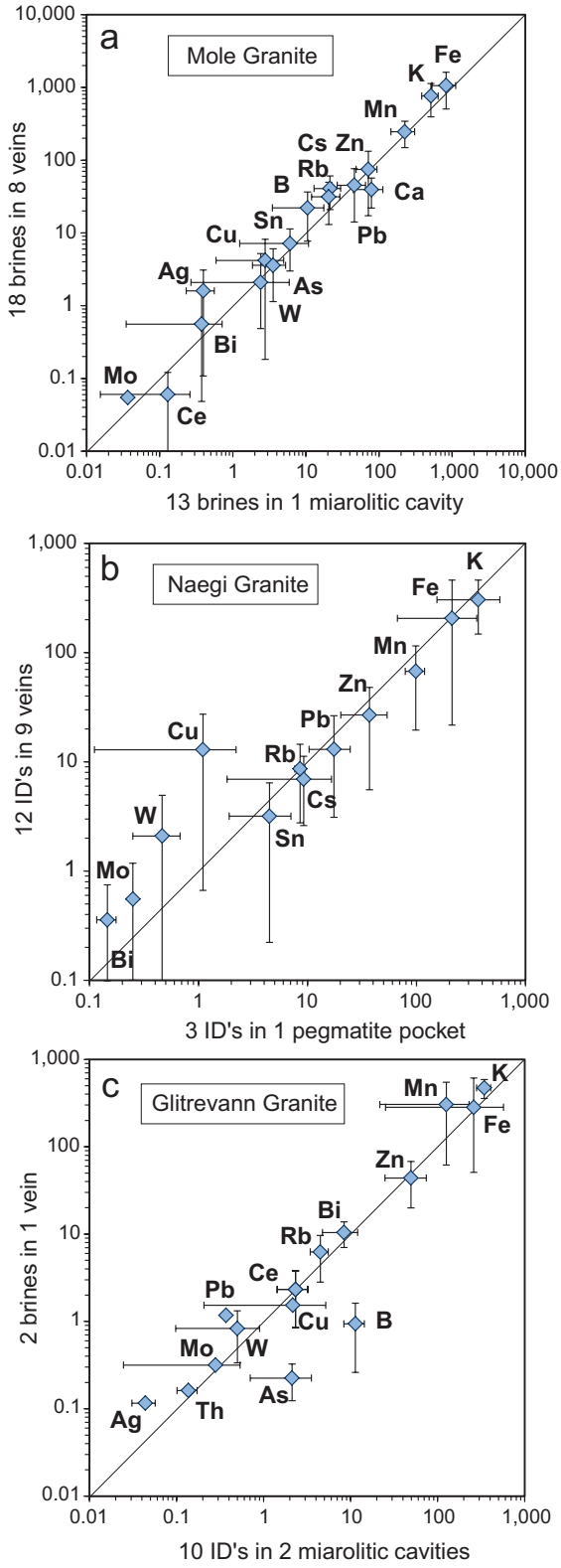

Fig. 12. Comparison of fluid inclusion compositions analyzed from miarolitic cavities vs. those analyzed from veins in the same pluton. (a). Brine compositions from 1 miarolitic cavity vs brine compositions from Sn-W-(Bi-Au) mineralized veins in the Mole Granite, Australia. (b). Composition of ID-type fluids from a pegmatite pocket vs. ID-type fluids from W-Sn-Bi mineralized veins in the Naegi granite, Japan. (c). Composition of ID-type fluids from miarolitic cavities vs. brine compositions from a vein in the Glitrevann granite, Norway.

cavities are compared with two brine assemblages from a weakly Mo mineralized vein (Fig. 12c). Also, here, most element abundances agree within uncertainty, except for B and As, which can be explained by element fractionation during vapor-brine separation (cf. Fig. 5). In summary, the results of these tests suggest that fluids trapped in miarolitic cavities are representative of potentially mineralizing fluids. Although miarolitic cavities develop at high degrees of magma crystallization and partly behave as closed systems at magmatic conditions (Audétat and Pettke, 2003), they seem to transform to open systems after the magma solidus is reached, allowing the passage of less-evolved fluids exsolving from deeper parts of the pluton.

Summary of selection criteria

To summarize, the following criteria were applied to select fluid compositions from large datasets: (1) the analyzed fluid inclusions should have been in a good state of preservation; (2) the fluid inclusions should have formed at high temperature (>450°C; preferably >500°C); (3) averages of multiple fluid inclusion analyses of fluid inclusion assemblages are preferred over measurements of single fluid inclusions; (3) to avoid bias toward occurrences from which a large number of data are available, a maximum four ID-type fluids plus four brines were selected per occurrence; and (5) based on the results of the numerical modeling, the selected fluids should cover the entire range of recorded Cs/Na ratios.

Results and Discussion

The full dataset comprising 169 different fluids from 14 barren intrusions, 12 Cu-(Mo, Au) mineralized intrusions, 10 Sn/W mineralized intrusions, two Mo mineralized intrusions, and one Th-U-REE- mineralized intrusion is provided in Appendix Table A1. Only the average concentration of each fluid inclusion assemblage is listed in this table because the corresponding standard deviation is usually very small compared to the concentration range covered by the entire data set (two to five orders of magnitude, depending on element). Graphs of Na normalized element abundances plotted against Cs/Na ratios are shown in Figures 13 and 14. Similar graphs showing the absolute element concentrations in ID-type fluids are provided in supplementary Figure A2. These graphs display the same trends as those in the Na normalized graphs (just with fewer data points) because no systematic differences in the salinity of magmatic bulk fluids exist between barren and variously mineralized intrusions (Fig. 4b).

If one takes a look at the Na normalized Sn abundances (Fig. 13a) it is striking that fluids analyzed from Sn/W mineralized intrusions are characterized by high Sn abundances compared to fluids analyzed from Mo-, Cu- or REE mineralized intrusions. Equally high Sn/Na ratios are observed only in some fluids from barren intrusions, which may be related to the fact that in the present comparison the fluids analyzed from barren and Sn/W mineralized intrusions are on average more evolved (according to their Cs/Na ratios) than the ones analyzed from Cu-, Mo- or REE mineralized intrusions. The correlation between high Sn/Na ratios and Sn mineralization becomes even more evident if one considers brine compositions only (Fig. 13b). These observations imply that high Sn/Na ratios in fluids (particularly in brines) are a strong indicator of Sn mineralization. Sn/Na ratios tend to increase with increasing Cs/Na ratios, suggesting that Sn gets enriched in the residual silicate melt during fractional crystallization. The situation for W is more complex (Fig. 13c). Normalized W abundances cover a wide range for both barren and Sn/W mineralized intrusions, but if one focuses on brines it is noticed that six out of the seven highest W/Na ratios stem from Sn/W mineralized intrusions (Fig. 13d). This could indicate that W deposits are principally produced from W-rich fluids, but that some of the analyzed fluids were already depleted in this element due to the high formation temperature of many tungsten ores (Audétat et al., 2000b; Hart, 2007). Similar to Sn, normalized W abundances tend to increase with increasing Cs/Na, suggesting that W commonly behaves incompatibly during fractional crystallization.

Normalized Cu abundances in ID-type fluids (Fig. 13e) tend to be high in fluids analyzed from Cu (Mo, Au) mineralized systems, but equally high Cu/Na ratios are observed also in certain fluids from barren intrusions, Sn/W mineralized intrusions, and Mo mineralized intrusions (Fig. 13e). It should be remembered, however, that the Cu content of ID-type fluid inclusions may have become altered by postentrapment diffusion of Cu into them (Lerchbaumer and Audétat, 2012). It may thus be safer to focus on brines only. If one does that (Fig. 13f), a different picture emerges, in which high Cu/Na ratios are almost exclusively confined to fluids from Cu (Mo, Au) mineralized systems, except for four data points from Mo mineralized systems. Notice that in contrast to Sn and W, the abundance of Cu tends to decrease with increasing Cs/Na, which reflects the generally compatible behavior of Cu during fractional crystallization.

Molybdenum abundances are relatively high in fluids from Mo mineralized systems, but similarly high abundances are observed also in fluids from Cu mineralized systems, barren systems, and Sn/W mineralized systems (Fig. 13g). This picture does not change if one considers brines only (Fig. 13h). Cerium abundances are high in the fluids analyzed from the U-Th-REE mineralized intrusion, but similarly Ce/Na ratios were found also in fluids analyzed from Mo mineralized intrusions, Sn/W mineralized intrusions, and barren intrusions (Fig. 14a). Since all four fluids analyzed from the U-Th-REE mineralized intrusion are brines, this picture does not change much if only brines are considered. The abundances of B and Bi generally increase with the abundance of Cs, and thus are highest in the barren and Sn/W mineralized intrusions (Fig. 14b, c). In contrast, the abundances of Pb, Zn, and Fe are rather constant and do not vary much as a function of Cs (Fig. 14d, e, f). Normalized Ag abundances scatter considerably but are generally high in fluids from Sn/W mineralized intrusions (Fig. 14g), whereas normalized sulfur abundances tend to be high in Cu (Mo, Au) mineralized intrusions and low in Sn/W mineralized intrusions (Fig. 14h). It should be noted that the abundances of base metals (Cu, Pb, and Zn) are generally much higher than those of Sn, W, and Mo, also in the fluids from Sn/W or Mo mineralized systems. This means that metal precipitation in the latter deposits was highly selective, which is evident also from the common regional metal zoning patterns around them (e.g., Sharp, 1978; Bookstrom, 1989; Robb, 2005). Normalized Cu abundances in brines from porphyry Cu (Mo, Au) systems are in most cases higher than

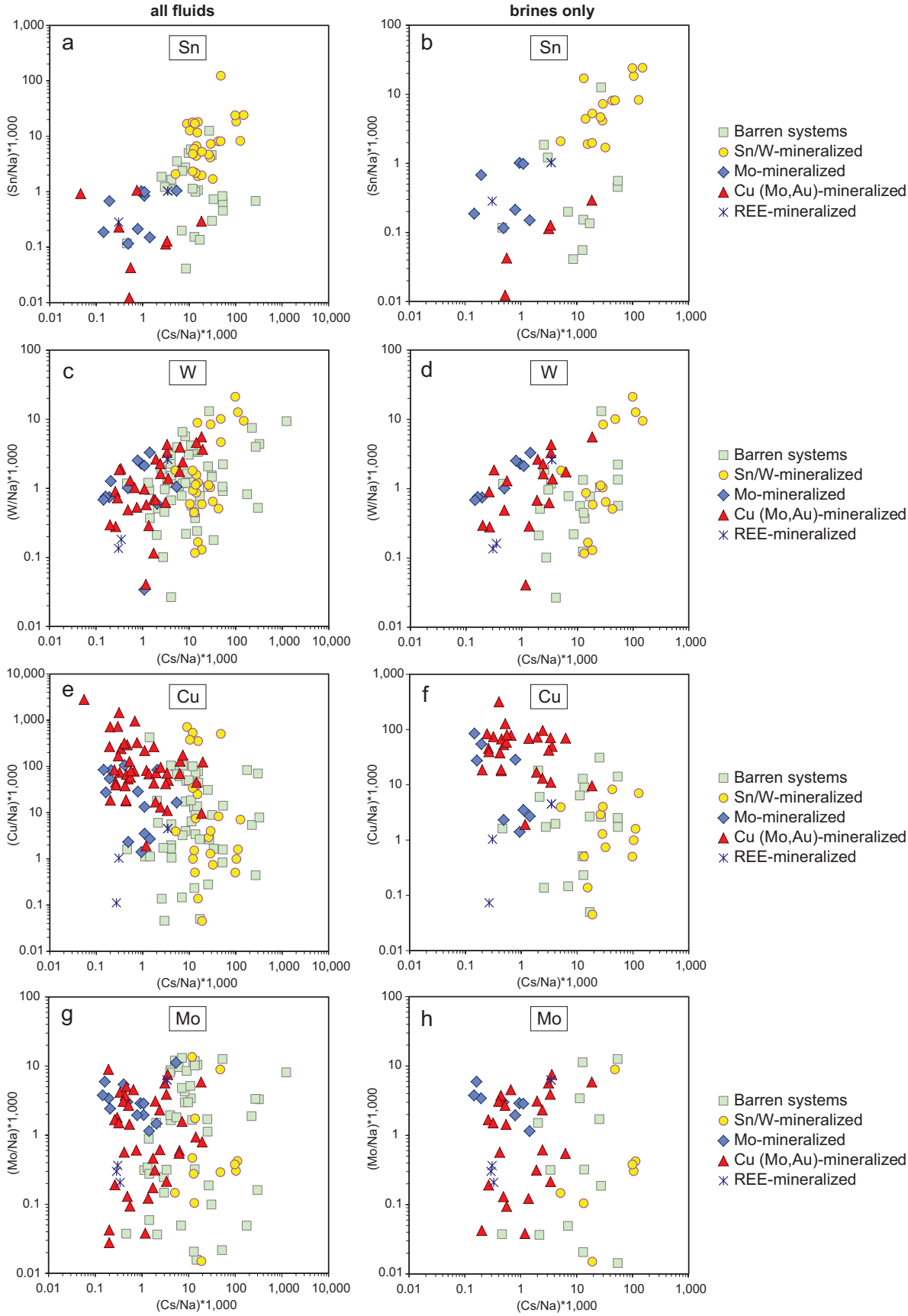

Fig. 13. Sodium normalized metal abundances in both ID-type and brine fluids (a, c, e, g), versus in brines only (b, d, f, h).

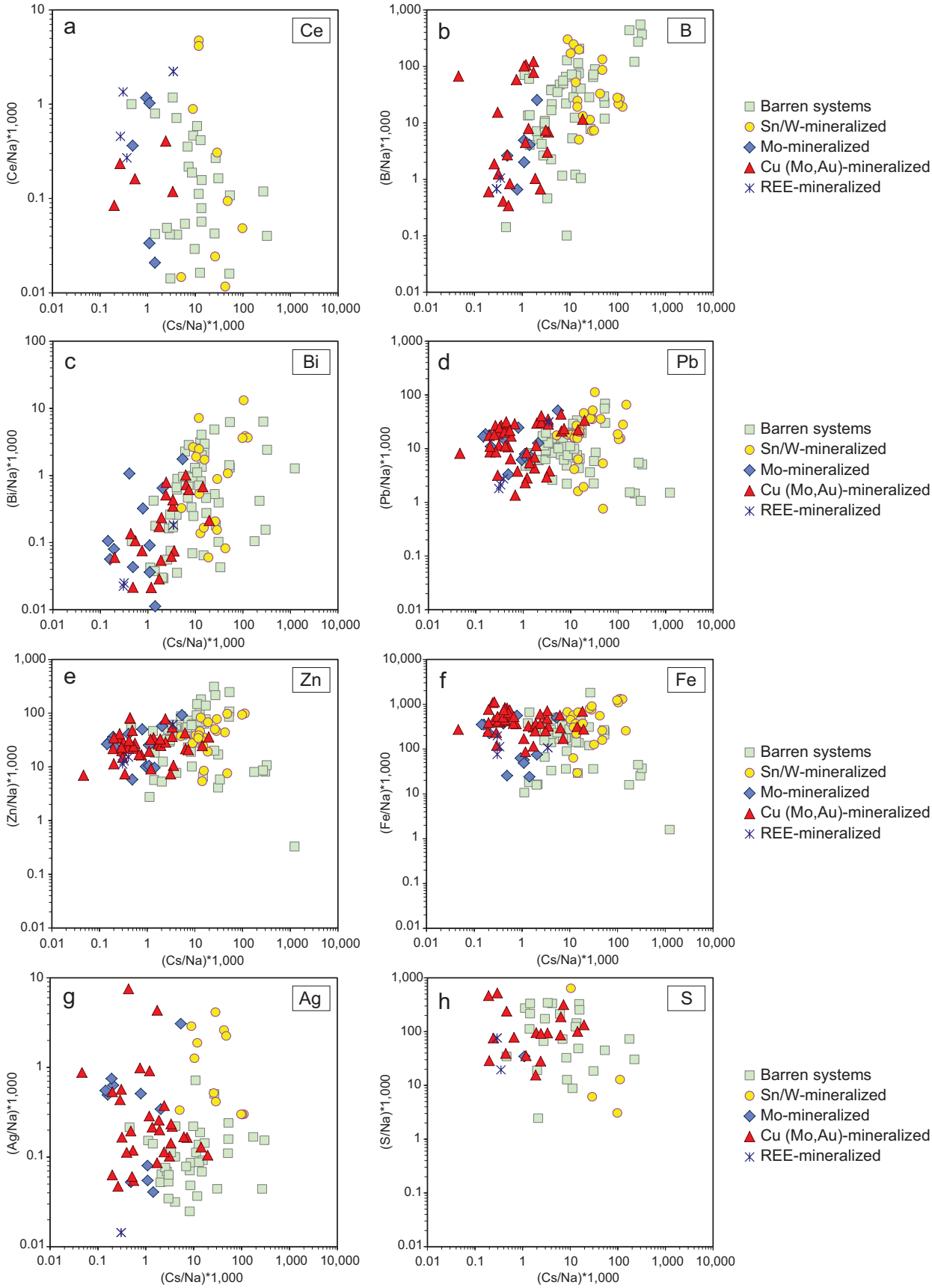

Fig. 14. Sodium normalized element abundances in both ID-type fluids and brines.

the corresponding Pb abundances, whereas Zn can be either more abundant or less abundant than Cu.

In summary, the results shown in Figures 13 and 14 reveal that positive correlations between the fluid metal content (normalized to Na) and the degree and type of mineralization exist for Sn, Cu, and potentially for W and REE, but not for Mo. These correlations are more pronounced in brines than in ID-type fluids, which supports the hypothesis that brines, although less abundant than ID- and/or vapor-type fluids at the scale of entire magmatic-hydrothermal systems, play a central role in ore deposition. The metal content of magmatic fluids is determined by (1) the metal content of the silicate melts from which they exsolved, and (2) by the fluid/melt partition coefficients. Of those two parameters, the latter likely shows less variability because the fluid/melt partition coefficients of most metals depend primarily on fluid salinity and there is only relatively little variation in the salinity of bulk fluids (i.e., of ID-type fluids) exsolved from barren and variously mineralized intrusions (Table 1). Therefore, the probable reason for the high Sn content of fluids in Sn/W mineralized intrusions is preenrichment of Sn in the silicate melt during fractional crystallization, as suggested by Lehmann (1990), Stemprok (1990), and subsequently demonstrated by means of melt inclusions by Webster et al. (1996, 1997) and Audétat et al. (2000b). Similarly, the comparatively high Cu content of the Cu (Mo, Au)-mineralizing fluids is likely due to a comparatively high Cu content in the associated magmas rather than due an anomalously high fluid/melt partition coefficient. However, it should be noticed that in the case of Cu the comparison to barren systems may not be valid because the barren intrusions in the present comparison tend to be more evolved than the average Cu (Mo, Au) mineralized intrusions. Hence, it is possible that less evolved, barren systems exist in which there are exsolved fluids with similarly high Cu contents as the fluids in Cu (Mo, Au) mineralized systems.

The fact that some fluids of barren intrusions have similarly high metal contents as fluids of mineralized intrusions (which is particularly true for Mo, W, Ce, Bi, Pb, and Zn) suggests that the mineralization potential of granitic intrusions is not just a function of the metal content of fluids but depends on other factors as well. A likely key factor is the efficiency of fluid extraction from the pluton, which depends itself on factors such as the intrusion shape, the depth of magma emplacement, the tectonic stress regime, and perhaps the mode of magma chamber construction and crystallization. Magma chambers that form at shallow depth ($\leq$3 km) are likely to erupt catastrophically in a caldera-forming event and thereby lose their ability to form ore deposits. Very deeply emplaced ($\geq$10–15 km) magma chambers, on the other hand, are unlikely to develop structures that promote focused fluid flow, such as apophyses, stockwork veins or breccia pipes. A flat-roofed, sill-like intrusion shape or a strongly compressional tectonic regime may also reduce the chance to develop structures that are required for focused fluid flow. Good chances for porphyry-type mineralization are predicted for large, ±equidimensional intrusions that are emplaced at 3- to 10-km depth and develop an apophysis, a breccia pipe, or a small volcanic conduit at some stage during their crystallization history (e.g., Sillitoe, 2010).

Conclusions

The present compilation confirms the finding of earlier studies, which showed that the salinity of magmatic bulk fluids typically lies between 5 and 15 wt % NaCl equiv in both barren and mineralized intrusions. The evolution of these fluids during cooling depends on intrusion depth: (1) in deep-seated intrusions (>6-km depth) the fluids stay in the single-phase field during the entire evolution from ~700° to ~400°C; (2) in intrusions emplaced at intermediate depth levels (4–6 km), which is typical for mineralized systems, the fluids start off in the single-phase field and later split into two phases (vapor + brine) within that temperature interval; (3) in shallow intrusions (<4 km-depth) the fluids are in the two-phase field already at the magmatic stage. To be able to include both ID-type fluids and brines in the comparison, element concentrations were normalized to Na. This approach is valid because no systematic difference exists in regard to the salinity of magmatic bulk fluids in barren versus mineralized intrusions. The Cs content of high-temperature (>450°C) fluids has been shown to be a measure of the fractionation degree of the magmas from which the fluids exsolved. In order to assess which fluids (Cs-rich vs. Cs-poor) are most representative of mineralizing fluids, a numerical model was developed that allows prediction at which stage of magma crystallization the largest amount of metal is able to leave the pluton. The model demonstrates that depending on metal, pressure, fluid/melt partition coefficient and bulk mineral-melt partition coefficient, the largest amount of metal may be extracted by early (i.e., Cs-poor) or by late (i.e., Cs-rich) fluids, and that it is not always the most metal rich fluids that extract the largest amount of metal from the cooling pluton. Consequently, for the comparison, high-temperature fluids were chosen over the entire range of recorded Cs concentrations.

The resulting graphs reveal that strongly positive correlations between the fluid metal content and the mineralization potential exist for Sn and Cu, weak positive correlations exist for W and REE, and none exist for Mo. This means that, at least with regard to Sn and Cu mineralization, but perhaps also with regard to W and REE mineralization, Na normalized metal abundances of high-temperature fluid inclusions could potentially be used as an exploration tool. However, the fact that high metal concentrations are observed also in fluids from some barren intrusions implies that the mineralization potential is also affected by additional factors, such as the size of the intrusion, its emplacement depth, its shape, and perhaps the tectonic stress regime. Mineralization-specific enrichments of selected metals exist also in the silicate melt (e.g., Audétat and Lowenstern, 2014), but a systematic comparison between barren and variously mineralized systems is still lacking.

Acknowledgments

I would like to express my gratitude to Chris Heinrich, Detlef Günther, Thomas Pettke, Hans Keppler, and Bob Bodnar for their great mentoring during the early stages of my career. For the present study I would like to thank Hubert Schulze and Raphael Njul for the preparation of thin sections, and Yuta Yoshie and Moritz Albrecht for allowing me to use data from their Ph.D. theses. Gleb Pokrovski, Matt Steele-MacInnis, and an anonymous reviewer are thanked for their excellent

reviews, and Jia Chang, Bertrand Rottier, and Daohan Zhang for stimulating discussions and comments on an early version of the manuscript.

REFERENCES

Albrecht, M., 2017, The role of the fluid composition in the formation of hydrothermal Sn-W ores: Insights from in situ analyses of fluid inclusions by UV-fs-LA-ICP-MS: Ph.D. thesis, University of Hannover, 160 p.

Allan, M.M., Yardley, B.W.D., Forbes, L.J., Shmulovich, K.I., Banks, D.A., and Shepherd, T.J., 2005, Validation of LA-ICP-MS fluid inclusion analysis with synthetic fluid inclusions: American Mineralogist, v. 90, p. 1767–1775.

Audétat, A., 2010, Source and evolution of molybdenum in the porphyry-Mo(-Nb) deposit at Cave Peak, Texas: Journal of Petrology, v. 51, p. 1739–1760.

Audétat, A., and Günther, D., 1999, Mobility and H_2O-loss from fluid inclusions in natural quartz crystals: Contributions to Mineralogy and Petrology, v. 137, p. 1–14.

Audétat, A., and Li, W., 2017, The genesis of Climax-type porphyry Mo deposits: Insights from fluid inclusions and melt inclusions: Ore Geology Reviews, v. 88, p. 436–460.

Audétat, A., and Lowenstern, J. B., 2014, Melt inclusions, *in* Scott, S. D., ed., Geochemistry of mineral deposits. Treatise on geochemistry, 2nd ed.: Oxford, Elsevier, v. 13, p. 143–173.

Audétat, A., and Pettke, T., 2003, The magmatic-hydrothermal evolution of two barren granites: A melt and fluid inclusion study of the Rito del Medio and Cañada Pinabete plutons in northern New Mexico (USA): Geochimica et Cosmochimica Acta, v. 67, p. 97–121.

Audétat, A., and Zhang, D., 2019, Abundances of S, Ga, Ge, Cd, In, Tl and 32 other major to trace elements in high-temperature (400–700°C) magmatic-hydrothermal fluids: Ore Geology Reviews, v. 109, p. 630–642.

Audétat, A., Günther, D., and Heinrich, C.A., 1998, Formation of a magmatic-hydrothermal ore deposit: Insights with LA-ICP-MS analysis of fluid inclusions: Science, v. 279, p. 2091–2094.

——2000a, Causes for large-scale metal zonation around mineralized plutons: Fluid inclusion LA-ICP-MS evidence from the Mole Granite, Australia: Economic Geology, v. 95, p. 1563–1581.

——2000b, Magmatic-hydrothermal evolution in a fractionating granite: A microchemical study of the Sn-W-F mineralized Mole Granite (Australia): Geochimica et Cosmochimica Acta, v. 64, p. 3373–3393.

Audétat, A., Pettke, T., Heinrich, C.A., and Bodnar, R.J., 2008, The composition of magmatic-hydrothermal fluids in barren and mineralized intrusions: Economic Geology, v. 103, p. 877–908.

Baline, L.M., 2007, Hydrothermal fluids and Cu-Au mineralization of the deep Grasberg porphyry deposit, Papua, Indonesia: M.Sc. thesis, University of Texas at Austin, 287 p.

Barnes, H.L., 1997, Geochemistry of hydrothermal ore deposits, 3rd ed.: New York, Wiley, 972 p.

Beane, R.E., and Bodnar, R.J., 1995, Hydrothermal fluids and hydrothermal alteration in porphyry copper deposits: Arizona Geological Society Digest, v. 20, p. 83–93.

Bodnar, R.J., Burnham, C.W., and Sterner, S.M., 1985, Synthetic fluid inclusions in natural quartz. III. Determination of phase equilibrium properties in the system H_2O-NaCl to 1000°C and 1500 bars: Geochimica et Cosmochimica Acta, v. 49, p. 1861–1873.

Bodnar, R.J., Lecumberri-Sanchez, P., Moncada, D., and Steele-MacInnis, M., 2014, Fluid inclusions in hydrothermal ore deposits: Treatise on Geochemistry, 2nd ed., v. 13, p. 119–142.

Bookstrom, A.A., 1989, The Climax-Alma granite batholith of Oligocene age and the porphyry molybdenum deposits of Climax, Colorado, U.S.A.: Engineering Geology, v. 27, p. 543–568.

Campbell, A.R., Banks, D.A., Randall, S.P., and Yardley, B.W.D., 1995, Geochemistry of Th-U-REE mineralizing magmatic fluids, Capitan Mountains, New Mexico: Economic Geology, v. 90, p. 1271–1287.

Chang, J., Li, J.W., and Audétat, A., 2018, Formation and evolution of multistage magmatic-hydrothermal fluids at the Yulong porphyry Cu-Mo deposit, eastern Tibet: Insights from LA-ICP-MS analysis of fluid inclusions: Geochimica et Cosmochimica Acta, v. 232, p. 181–205.

Cline, J.S., 1995, Genesis of porphyry copper deposits: The behavior of water, chloride and copper in crystallizing melts: Arizona Geological Society Digest, v. 20, p. 69–82.

Cline, J.S., and Bodnar, R.J., 1991, Can economic porphyry copper mineralization be generated by a typical calc-alkaline melt?: Journal of Geophysical Research, v. 96, p. 8113–8126.

Driesner, T., and Heinrich, C.A., 2007, The system H_2O-NaCl. Part I: Correlation formulae for phase relations in temperature-pressure-composition space from 0 to 1000°C, 0 to 5000 bar, and 0 to 1 X_{NaCl}: Geochimica et Cosmochimica Acta, v. 71, p. 4880–4901.

Fall, A., and Bodnar, R.J., 2018, How precisely can the temperature of a fluid event be constrained using fluid inclusions?: Economic Geology, v. 113, p. 1817–1843.

Frezzotti, M.L., Tecce, F., and Casagli, A., 2012, Raman spectroscopy for fluid inclusion analysis: Journal of Geochemical Exploration, v. 112, p. 1–20.

Goldstein, R.H., 2003, Petrographic analysis of fluid inclusions: Mineralogical Association of Canada, Short Course Series, v. 32, p. 9–53.

Goldstein, R.H., and Reynolds, T.J., 1994, Systematics of fluid inclusions in diagenetic minerals: Tulsa, Oklahoma, Society for Sedimentary Geologists, 199 p.

Graupner, T., Brätz, H., and Klemd, R., 2005, LA-ICP-MS micro-analysis of fluid inclusions in quartz using a commercial Merchantek 266 nm Nd:YAG laser: A pilot study: European Journal of Mineralogy, v. 17, p. 93–102.

Guillong, M., Latkoczy, C., Seo, J.H., Günther, D., and Heinrich, C.A., 2008, Determination of sulfur in fluid inclusions by laser ablation ICP-MS: Journal of Analytical Atomic Spectrometry, v. 23, p. 1581–1589.

Günther, D., Audétat, A., Frischknecht, R., and Heinrich, C.A., 1998, Quantitative analysis of major, minor and trace elements in fluid inclusions using laser ablation-inductively coupled plasma-mass spectrometry (LA-ICP-MS): Journal of Analytical Atomic Spectrometry, v. 13, p. 263–270.

Hart, C.J.R., 2007, Reduced intrusion-related gold systems: Geological Association of Canada Special Publication 5, p. 95–112.

Hedenquist, J.W., and Lowenstern, J.B., 1994, The role of magmas in the formation of hydrothermal ore deposits: Nature, v. 370, p. 519–527.

Hedenquist, J.W., and Richards, J.P., 1998, The influence of geochemical techniques on the development of genetic models for porphyry copper deposits: Reviews in Economic Geology, v. 10, p. 235–256.

Heinrich, C.A., 1990, The chemistry of hydrothermal tin(-tungsten) ore deposition: Economic Geology, v. 85, p. 457–481.

——1995, Geochemical evolution and hydrothermal mineral deposition in Sn (-W-base metal) and other granite-related ore systems: Some conclusions from Australian examples: Mineralogical Association of Canada, Short Course Series, v. 23, p. 203–220.

——2005, The physical and chemical evolution of low- to medium-salinity magmatic fluids at the porphyry to epithermal transition: A thermodynamic study: Mineralium Deposita, v. 39, p. 864–889.

Heinrich, C.A., Ryan, C.G., Mernagh, T.P., and Eadington, P.J., 1992, Segregation of ore metals between magmatic brine and vapor: A fluid inclusion study using PIXE microanalysis: Economic Geology, v. 87, p. 1566–1583.

Heinrich, C.A., Günther, D., Audétat, A., Ulrich, T., and Frischknecht, R., 1999, Metal fractionation between magmatic brine and vapor, determined by microanalysis of fluid inclusions: Geology, v. 27, p. 755–758.

Heinrich, C.A., Pettke, T., Halter, W., Aigner-Torres, M., Audétat, A., Günther, D., Hattendorf, B., Bleiner, D., Guillong, M., and Horn, I., 2003, Quantitative multi-element analysis of minerals, fluid and melt inclusions by laser-ablation inductively-coupled-plasma mass-spectrometry: Geochimica et Cosmochimica Acta, v. 67, p. 3473–3496.

Heinrich, C.A., Driesner, T., Stefánsson, A., and Seward, T.M., 2004, Magmatic vapour contraction and the transport of gold from the porphyry environment to epithermal deposits: Geology, v. 32, p. 761–764.

Heinrich, C.A., Meier, D., Erni, M., VonQuadt, A., and Márquez-Zavalía, F., 2011, Life-times and scales of Cu-Au-mineralizing magmatic-hydrothermal processes: Farallón Negro, Argentina [ext. abs.]: Society for Geology Applied to Mineral Deposits (SGA), Biennial Meeting, 11th, Antofagasta, Chile, Extended Abstracts, 4 p.

Johannes, W., and Holtz, F., 1996, Petrogenesis and experimental petrology of granitic rocks: Berlin, Springer, 335 p.

Kesler, S.E., and Simon, A.C., 2015, Mineral resources, economics and the environment, 2nd ed.: Cambridge, Cambridge University Press, 434 p.

Klemm, L., Pettke, T., Heinrich, C.A., and Campos, E., 2007, Hydrothermal evolution of the El Teniente deposit, Chile: Porphyry Cu-Mo ore deposition from low-salinity magmatic fluids: Economic Geology, v. 102, p. 1021–1045.

Klemm, L.M., Pettke, T., and Heinrich, C.A., 2008, Fluid and source magma evolution of the Questa porphyry Mo deposit, New Mexico, USA: Mineralium Deposita, v. 43, p. 533–552.

Kouzmanov, K., and Pokrovski, G.S., 2012, Hydrothermal controls on metal distribution in porphyry Cu (-Mo-Au) systems: Society of Economic Geologists Special Publication 16, p. 573–618.

Kurosawa, M., Ishii, S., and Sasa, K., 2010, Trace-element compositions of single fluid inclusions in the Kofu granite, Japan: Implications for compositions of granite-derived fluids: Island Arc, v. 19, p. 40–59.

Kurosawa, M., Sasa, K., Shin, K.-C., and Ishii, S., 2016, Trace-element compositions and Br/Cl ratios of fluid inclusions in the Tsushima granite, Japan: Significance for formation of granite-derived fluids: Geochimica et Cosmochimica Acta, v. 182, p. 216–239.

Lambrecht, G., and Diamond, L.W., 2014, Morphological ripening of fluid inclusions and coupled zone-refining in quartz crystals revealed by cathodoluminescence imaging: Implications for CL-petrography, fluid inclusion analysis and trace-element geothermometry: Geochimica et Cosmochimica Acta, v. 141, p. 381–406.

Landtwing, M.R., Pettke, T., Halter, W.E., Heinrich, C.A., Redmond, P.B., Einaudi, M.T., and Kunze, K., 2005, Copper deposition during quartz dissolution by cooling magmatic-hydrothermal fluids: The Bingham porphyry: Earth and Planetary Science Letters, v. 235, p. 229–243.

Landtwing, M.R., Furrer, C., Redmond, P.B., Pettke, T., Guillong, M., and Heinrich, C.A., 2010, The Bingham Canyon porphyry Cu-Mo-Au deposit. III. Zoned copper-gold ore deposition by magmatic vapor expansion: Economic Geology, v. 105, p. 91–118.

Lehmann, B., 1990, Metallogeny of tin: Berlin, Springer, 211 p.

Lerchbaumer, L., and Audétat, A., 2012, High Cu concentrations in vapor-type fluid inclusions: An artifact?: Geochimica et Cosmochimica Acta, v. 88, p. 255–274.

——2013, The metal content of silicate melts and aqueous fluids in subeconomically Mo mineralized granites: Implications for porphyry Mo genesis: Economic Geology, v. 108, p. 987–1013.

Luth, W.C., Jahns, R.H., and Tuttle, O.F., 1964, The granite system at pressures of 4 to 10 kbars: Journal of Geophysical Research, v. 69, p. 759–773.

Mavrogenes, J.A., and Bodnar, R.J., 1994, Hydrogen movement into and out of fluid inclusions in quartz: Experimental evidence and geologic implications: Geochimica et Cosmochimica Acta, v. 58, p. 141–148.

Mavrogenes, J.A., Bodnar, R.J., Anderson, A.J., Bajt, S., Sutton, S.R., and Rivers, M.L., 1995, Assessment of the uncertainties and limitations of quantitative elemental analysis of individual fluid inclusions using synchrotron X-ray fluorescence (SXRF): Geochimica et Cosmochimica Acta, v. 59, p. 3987–3995.

Nash, J.T., 1976, Fluid-inclusion petrology—data from porphyry copper deposits and applications to exploration: U.S. Geological Survey Professional Paper 907–D, 16 p.

Naumov, V.B., and Kamenetsky, V.S., 2006, Silicate and slat melts in the genesis of the Industrial'noe tin deposit: Evidence from inclusions in minerals: Geochemistry International, v. 44, p. 1181–1190.

Olsen, K.I., and Griffin, W.L., 1984, Fluid inclusion studies of the Drammen granite Oslo paleorift, Norway: Contributions to Mineralogy and Petrology, v. 87, p. 1–14.

Pettke, T., 2008, Analytical protocols for element concentration and isotope ratio measurements in fluid inclusions by LA-(MC-)ICP-MS: Mineralogical Association of Canada, Short Course Series, v. 40, p. 189–217.

Pitzer, K.S., and Pabalan, R.T., 1986, Thermodynamics of NaCl in steam: Geochimica et Cosmochimica Acta, v. 50, p. 1445–1454.

Piwinskii, A.J., and Wyllie, P.J., 1968, Experimental studies of igneous rock series: A zoned pluton in the Wallowa batholith, Oregon: Journal of Geology, v. 76, p. 205–234.

Pokrovski, G.S., Borisova, A.Y., and Bychkov, A.Y., 2013, Speciation and transport of metals and metalloids in geological vapors: Reviews in Mineralogy and Geochemistry, v. 76, p. 165–218.

Pudack, C., Halter, W.E., Heinrich, C.A., and Pettke, T., 2009, Evolution of magmatic vapor to gold-rich epithermal liquid: the porphyry to epithermal transition at Nevados de Famatina, northwest Argentina: Economic Geology, v. 104, p. 449–477.

Redmond, P.B., Einaudi, M.T., Inan, E.E., Landtwing, M.R., and Heinrich, C.A., 2004, Copper deposition by fluid cooling in intrusion-centered systems: New insights from the Bingham porphyry ore deposits, Utah: Geology, v. 32, p. 217–220.

Robb, L., 2005, Introduction to ore-forming processes: Oxford, Blackwell Publishing, 373 p.

Roedder, E., 1984, Fluid inclusions: Washington, DC, Mineralogical Society of America, 644 p.

Rusk, B., 2012, Cathodoluminescent textures and trace elements in hydrothermal quartz, *in* Götze, J., Möckel, R., eds., Quartz: Deposits, mineralogy and analytics: Berlin, Springer, p. 307–329.

Rusk, B.G., Reed, M.H., Dilles, J.H., Klemm, L., and Heinrich, C.A., 2004, Compositions of magmatic hydrothermal fluids determined by LA-ICP-MS of fluid inclusions from the porphyry copper-molybdenum deposit at Butte, MT: Chemical Geology, v. 210, p. 173–199.

Rusk, B.G., Reed, M.H., and Dilles, J.H., 2008, Fluid inclusion evidence for magmatic-hydrothermal fluid evolution in the porphyry copper-molybdenum deposit at Butte, Montana: Economic Geology, v. 103, p. 307–334.

Samson, I., Anderson, A., and Marshall, D., 2003, Fluid inclusions: Analysis and interpretation: Mineralogical Association of Canada, Short Course Series, v. 32, 374 p.

Seo, J.H., and Heinrich, C.A., 2013, Selective copper diffusion into quartz-hosted vapor inclusions: Evidence from other host minerals, driving forces, and consequences for Cu-Au ore formation: Geochimica et Cosmochimica Acta, v. 113, p. 60–69.

Seo, J.H., Guillong, M., and Heinrich, C.A., 2009, The role of sulfur in the formation of magmatic-hydrothermal copper-gold deposits: Earth and Planetary Science Letters, v. 282, p. 323–328.

——2012, Separation of molybdenum and copper in porphyry deposits: the roles of sulfur, redox, and pH in ore mineral deposition at Bingham Canyon: Economic Geology, v. 107, p. 333–356.

Seo, J.H., Guillong, M., Aerts, M., Zajacz, Z., and Heinrich, C.A., 2011, Microanalysis of S, Cl, and Br in fluid inclusions by LA-ICP-MS: Chemical Geology, v. 284, p. 35–44.

Sharp, J.E., 1978, A molybdenum mineralized breccia pipe complex, Redwell basin, Colorado: Economic Geolology, v. 73, p. 369–382.

Shepherd, T.J., Rankin, A.H., and Alderton, D.H.M., 1985, A practical guide to fluid inclusion studies: London, Blackie, 239 p.

Shinohara, H., Iiyama, J.T., and Matsuo, S., 1989, Partition of chlorine compounds between silicate melt and hydrothermal solutions, I: Partition of NaCl-KCl: Geochimica et Cosmochimica Acta, v. 53, p. 2617–2630.

Sillitoe, R.H., 2010, Porphyry copper systems: Economic Geology, v. 105, p. 3–41.

Stefanova, E., Driesner, T., Zajacz, Z., Heinrich, C.A., Petrov, P., and Vasilev, Z., 2014, Melt and fluid inclusions in hydrothermal veins: The magmatic to hydrothermal evolution of the Elatsite porphyry Cu-Au deposit, Bulgaria: Economic Geology, v. 109, p. 1359–1381.

Stemprok, M., 1990, Solubility of tin, tungsten and molybdenum oxides in felsic magmas: Mineralium Deposita, v. 25, p. 205–212.

Ulrich, T., Günther, D., and Heinrich, C.A., 1999, Gold concentrations of magmatic brines and the metal budget of porphyry copper deposits: Nature, v. 399, p. 676–679.

——2002, The evolution of a porphyry Cu-Au deposit, based on LA-ICP-MS analysis of fluid inclusions: Bajo de la Alumbrera, Argentina: Economic Geology, v. 97, p. 1889–1920.

Webster, J.D., 1992, Water solubility and chloride partitioning in Cl-rich granitic systems: Effects on melt composition at 2 kbar and 800°C: Geochimica et Cosmochimica Acta, v. 56, p. 679–687.

Webster, J.D., Burt, D.M., and Aguillon, R.A., 1996, Volatile and lithophile trace-element geochemistry of Mexican tin rhyolite magmas deduced from melt inclusions: Geochimica et Cosmochimica Acta, v. 60, p. 3267–3284.

Webster, J.D., Thomas, R., Rhede, D., Förster, H.J., and Seltmann, R., 1997, Melt inclusions in quartz from an evolved peraluminous pegmatite: Geochemical evidence for strong tin enrichment in fluorine-rich and phosphorous-rich residual liquids: Geochimica et Cosmochimica Acta, v. 61, p. 2589–2604.

Williams-Jones, A.E., and Heinrich, C.A., 2005, Vapor transport of metals and the formation of magmatic-hydrothermal ore deposits: Economic Geology, v. 100, p. 1287–1312.

Wilson, J.W.J., Kesler, S.E., Cloke, P.L., and Kelly, W.C., 1980, Fluid inclusion geochemistry of the Granisle and Bell porphyry copper deposits, British Columbia: Economic Geology, v. 75, p. 45–61.

Yoshie, Y., 2012, Hydrothermal evolution of ilmenite-series granite in the inner zone of SW Japan: Ph.D. thesis, Ibaraki, Japan, University of Tsukuba, 54 p. (in Japanese).

Zajacz, Z., Halter, W. E., Pettke, T., and Guillong, M., 2008, Determination of fluid/melt partition coefficients by LA-ICPMS analysis of co-existing fluid and silicate melt inclusions: Controls on element partitioning: Geochimica et Cosmochimica Acta, v. 72, p. 2169–2197.

Zhang, D., and Audétat, A., 2018, Magmatic-hydrothermal evolution of the barren Huangshan pluton, Anhui province, China: A melt and fluid inclusion study: Economic Geology, v. 113, p. 803–824.

Andreas Audétat is a senior scientist at the Bavarian Geoinstitute in Bayreuth, Germany. He received his Ph.D. degree at ETH Zürich in 1999, followed by a two-year postdoctoral study at Virginia Tech. His research revolves mostly around magmatic-hydrothermal ore deposits, fluid inclusions, melt inclusions, LA-ICP-MS and thermobarometry, and includes both studies on natural samples as well as experimental studies.